

Double layer electric fields aiding the production of energetic flat-top distributions and superthermal electrons within the exhausts from magnetic reconnection.

J. Egedal

Department of Physics, University of Wisconsin-Madison, Madison, Wisconsin 53706, USA

W. Daughton and A. Le

Los Alamos National Laboratory, Los Alamos, New Mexico 87545, USA

A. L. Borg

Norwegian Meteorological Institute, Blindern, 0313 Oslo, Norway

(Dated: February 1, 2022)

Using a kinetic simulation of magnetic reconnection it was recently shown that magnetic-field-aligned electric fields (E_{\parallel}) can be present over large spatial scales in reconnection exhausts. The largest values of E_{\parallel} are observed within double layers. The existence of double layers in the Earth's magnetosphere is well documented. In our simulation their formation is triggered by large parallel streaming of electrons into the reconnection region. These parallel electron fluxes are required for maintaining quasi-neutrality of the reconnection region and increase with decreasing values of the normalized electron pressure upstream of the reconnection region, $\beta_{e\infty} = 2\mu_0 n_{e\infty} T_{e\infty} / B_{\infty}^2$. A threshold ($\beta_{e\infty} < 0.02$) is derived for strong double layers to develop. We also document how the electron confinement, provided in part by the structure in E_{\parallel} , allows sustained energization by perpendicular electric fields (E_{\perp}). The energization is a consequence of the confined electrons' chaotic orbital motion that includes drifts aligned with the reconnection electric field. The level of energization is proportional to the initial particle energy and therefore is enhanced by the initial energy boost of the acceleration potential, $e\Phi_{\parallel} = e \int_x^{\infty} E_{\parallel} dl$, acquired by electrons entering the region. The mechanism is effective in an extended region of the reconnection exhaust allowing for the generation of superthermal electrons in reconnection scenarios, including those with only a single x-line. An expression for the phase-space distribution of the superthermal electrons is derived, providing an accurate match to the kinetic simulation results. The numerical and analytical results agree with detailed spacecraft observations recorded during reconnection events in the Earth's magnetotail.

I. INTRODUCTION

It is widely believed that magnetic reconnection energizes electrons and is the source of superthermal electrons observed during solar flare events [1] and through *in situ* measurements in the Earth's magnetosphere [2]. Several previous studies of reconnection conclude that the dissipation sites (where electrons are energized) are limited to electron scale regions and are insufficient in size to account for the large scale electron energization. To circumvent this conundrum recent models have invoked the possibility of multiple reconnection locations and flux-rope formation, which can facilitate energy release in a larger spatial volume and thereby help energize the large number of electrons required by observations [3–6].

While there exists clear evidence of magnetic flux-ropes forming in the Earth's magnetosphere, these flux-ropes do not appear to be volume filling such that energization at multiple x-lines becomes effective [7, 8]. This suggests that energization within the exhaust from a single x-line needs to be efficient to account for the extensive energization levels recorded experimentally. We therefore revisit electron energization in single x-line reconnection and find that superthermal electrons are produced over large spatial scales in the single x-line reconnection exhaust when the total pressure of the plasma upstream of the

reconnection region is dominated by the magnetic field ($\beta_{e\infty} = 2\mu_0 p_{e\infty} / B_{\infty}^2 \ll 1$). In our kinetic simulation, a key to the strong electron energization is the break-down of adiabatic electron dynamics along the magnetic field lines, which, we find, is likely to occur when $\beta_{e\infty} < 0.02$.

The documented heating mechanism and non-adiabatic parallel electron dynamics lead to the formation of strong magnetic field, aligned (parallel) electric fields, E_{\parallel} . These structures are consistent with double layers, where local charge separation generates strong parallel electric fields [9–11]. The double layers provide an initial energization of electrons streaming into the reconnection region (and exhaust) along field lines. In addition, the double layer E_{\parallel} helps confine the electrons within the reconnection region, allowing for further energization by the reconnection electric field over the duration of multiple electron bounce orbits. The resulting electron distribution functions have characteristic signatures shaped by the interplay between the parallel and perpendicular electric fields during the energization process, which compare favorably to electron distributions observed *in situ* by spacecraft in the Earth's magnetotail [2, 12–14]. As is the case for the magnetotail, $\beta_{e\infty}$ is also believed to be small upstream of reconnection sites associated with solar flares [15], where the electron confinement provided by E_{\parallel} may also be important to explain

the long lifetime of hard X-ray sources at flare loop-tops [1, 16].

In previous work [13, 17, 18] we have mostly analyzed scenarios including a guide magnetic field sufficient in strength that the magnetic moments, $\mu = m_e v_\perp^2 / (2B)$, of the electrons are conserved, yielding adiabatic (time reversible) electron dynamics for both the parallel and perpendicular electron dynamics. Here we consider anti-parallel reconnection, which includes unmagnetized chaotic electron behavior in the reconnection exhaust leading to irreversible electron dynamics. More important for the energization process, however, is the aforementioned break-down of the adiabatic electron dynamics parallel to the magnetic field, causing the formation of large scale E_\parallel regions. The spatial extent of these regions is not tied to kinetic scales and expands with the reconnection exhaust. This suggests that the presented heating mechanism may be applicable to systems like solar flares, which are much larger than the simulation domain [14].

The paper is organized as follows: In Sec. II we discuss the formation of strong double layers, which form along the reconnection separators. The double layers are responsible in part for the confinement of electrons in the exhaust and we derive a threshold for their development. In Sec. III we consider properties of the exhaust where pitch angle mixing is effective, and derive the rate for the energization of electrons trapped in the exhaust. In Sec. IV we investigate the electron distributions that form within the exhaust, providing an explanation for the observed electron flat-top distributions. In addition, a model is derived for the superthermal electrons which is in good agreement with the kinetic simulations results. In Sec. V the numerical and theoretical results are compared to spacecraft observations and the paper is concluded in Sec. VI.

II. ELECTRON HOLES, AND DOUBLE LAYERS

A. Electron pressure anisotropy, the acceleration potential, Φ_\parallel , and a condition for adiabatic electrons

In this paper we document and analyze numerical simulation results obtained with the VPIC fully kinetic plasma simulation code [19], implementing a configuration with $\beta_{e\infty} = 0.003$. The two-dimensional simulation is initialized with a Harris neutral sheet, and open boundary conditions are employed in the x and z directions. The initial particle distributions include counter-drifting Maxwellian ion and electron populations localized to support the Harris current layer. In addition, a separate background density is included, resulting in a total density profile $n(z) = n_0 \text{sech}^2(z/d_i) + n_\infty$, where n_0 is the central Harris density, n_∞ is a uniform background density and $n_\infty/n_0 = 0.05$ for this simulation. The ion-to-electron temperature ratio of the Harris population is $T_{i0}/T_{e0} = 5$, whereas the temperatures, $T_{i\infty}$

and $T_{e\infty}$, for the uniform background populations have the same ratio, but are a factor of three colder for both species. Lengths are normalized by the ion $d_i = c/\omega_{pi}$ based on the Harris sheet density n_0 , in a domain size of $L_x \times L_z = 320d_i \times 30d_i$. Other parameters are $m_i/m_e = 400$, $T_{i\infty} = m_e c^2/29$ and $T_{e\infty} = m_e c^2/144$, and $\omega_{pe}/\Omega_{ce} = 2$, where $\Omega_{ce} = eB_\infty/(m_e c)$. The simulation data presented in Ref. [14] were also from this run, but here we provide a more in depth analysis and refined understanding of the numerical results.

Fig. 1 shows the profiles of the electron pressure anisotropy p_\parallel/p_\perp and the acceleration potential for a relatively early stage of the reconnection process, $t\Omega_{ci} = 31$. Here Φ_\parallel is defined as

$$\Phi_\parallel = \int_x^\infty E_\parallel dl, \quad (1)$$

and is a pseudo potential which measures the integrated parallel electric field E_\parallel along the magnetic field lines. Because of the large electron thermal speed the magnetic field lines can often be considered stationary during a single electron transit [18]. Thus, $e\Phi_\parallel$ characterizes the energy that electrons acquire in their free streaming along magnetic field lines into the reconnection region [20].

In Fig. 1, the relatively large pressure anisotropy and large values of $e\Phi_\parallel/T_{e\infty}$ in the inflow are accurately described by the self-consistent adiabatic electron model derived in Refs. [13, 17, 18]. The model provides equations of state (EOS) for the electron pressure components $p_\parallel = p_\parallel(n, B)$ and $p_\perp = p_\perp(n, B)$. For anti-parallel reconnection the EOS are applicable to the inflow region where the electron magnetic moments, $\mu = m_e v_\perp^2 / (2B)$, are conserved. The model includes the non-linear effects of electron trapping by the magnetic mirror force and by Φ_\parallel . For the present geometry with $e\Phi_\parallel/T_{e\infty} \simeq 18$, the trapped electrons dominate the properties of the electron fluid, and in this limit the electron pressure components $p_\parallel \propto n^3/B^2$ and $p_\perp \propto nB$ resemble the CGL scalings [21]. In addition to the EOS, the model also yields the self-consistent values of $\Phi_\parallel = \Phi_\parallel(n, B)$.

Although the EOS do not apply to the electron diffusion region where the electrons become unmagnetized, through a momentum balance analysis of the electron layer it is shown that the EOS regulate the integrated current across the layer [22, 23]. Another result of the momentum balance analysis in Ref. [22] is a scaling law for the magnitude of Φ_\parallel expected just upstream of the electron diffusion region:

$$\left(\frac{e\Phi_\parallel}{T_{e\infty}} \right) \approx \frac{1}{2} \left[\left(\frac{4\tilde{n}}{\beta_{e\infty}} \right)^{1/4} - \frac{1}{2} \right]^2, \quad (2)$$

where the predicted values of $e\Phi_\parallel/T_{e\infty}$ become large at small values of $\beta_{e\infty}$. Here $\tilde{n} = n/n_\infty$ and $\beta_{e\infty} = 2\mu_0 n_\infty T_{e\infty}/B_\infty^2$ is the normalized electron pressure upstream of the reconnecting current sheet.

Beside the break-down of the magnetic moment as an invariant, a second mechanism also causes the adiabatic

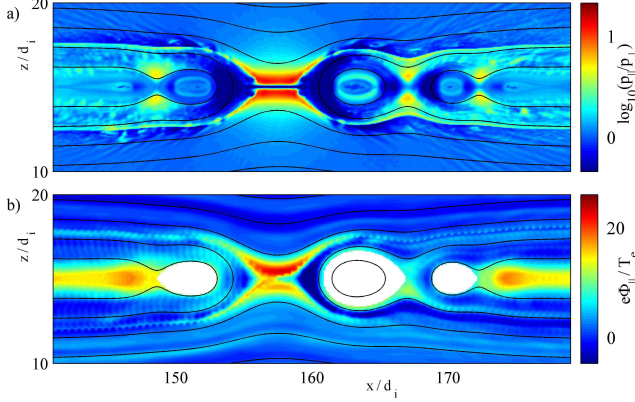


FIG. 1: (a-c): Color contours of constant pressure anisotropy $\log_{10}(p_{\parallel}/p_{\perp})$, and acceleration potential $e\Phi_{\parallel}/T_{e\infty}$. The magnetic field lines inside the island do not reach the ambient plasma and the acceleration potential, Φ_{\parallel} , is thus undefined within the areas left “white” in (b).

EOS to become invalid. This second mechanism is related to non-adiabatic effects in the parallel particle motion, and occurs at small values of $\beta_{e\infty}$. To estimate the critical value of $\beta_{e\infty}$ marking the transition to the non-adiabatic regime, we note that one important requirement for adiabatic parallel behavior is that changes in Φ_{\parallel} for a flux-tube moving into the reconnection region must be small during an electron transit through the region. To quantify this condition we revisit the derivation of the adiabatic model in Ref. [18], where a key element for solving the drift kinetic equation is an assumed ordering

$$\nabla_{\parallel} \sim \frac{1}{L}, \quad \nabla_{\perp} \sim \frac{1}{D}, \quad \frac{\partial}{\partial t} \sim \frac{v_D}{D},$$

$$\frac{D}{L} \sim \delta, \quad \frac{v_D}{v_{te\infty}} \sim \delta^2.$$

Here D and L are the typical length scales across and along the reconnection region, respectively, with $D/L \simeq 1/10$. The ratio between the electron drift speed $v_D \simeq 0.1v_A$ and the thermal speed is small $v_D/v_{te\infty} \simeq 1/400$ for $\beta_{e\infty} = 1$, but increases with decreasing values of $\beta_{e\infty}$.

The adiabatic solution in Ref. [18] corresponds to the limit where only electrons with small parallel energy may become trapped. This requires that during an electron transit time $\tau \simeq L/v_{te\infty}$ the changes in the magnetic and electric well (trapping electrons) must be small compared to $T_{e\infty}$. If this condition is not satisfied the parallel electron behavior may become non-adiabatic. Following Eq. 13 of Ref. [18], the condition for adiabatic dynamics

is then

$$\begin{aligned} T_{e\infty} &> \mu \frac{\partial B}{\partial t} \tau + e \frac{\partial E_{\parallel}}{\partial t} \tau L \\ &> \mu B \frac{v_D}{D} \frac{L}{v_{te\infty}} + e E_{\parallel} \frac{v_D}{D} \frac{L}{v_{te\infty}} L \\ &> \frac{v_A}{v_{te\infty}} (T_{e\infty} + e\Phi_{\parallel}) \quad , \end{aligned} \quad (3)$$

where we have used $v_A \simeq v_D L/D$. For the low values of $\beta_{e\infty}$ and assuming $\tilde{n} = 1$, Eq. (2) is approximately $e\Phi_{\parallel}/T_{e\infty} = 1/\sqrt{\beta_{e\infty}} (\gg 1)$. Furthermore, because $v_A^2/v_{te\infty}^2 = m_e/(m_i\beta_{e\infty})$, Eq. (3) may be written as $\beta_{e\infty} > \sqrt{m_e/m_i}$, as required to ensure parallel adiabatic behavior. Thus, we expect non-adiabatic parallel behavior in the inflow (and along the separators) for

$$\beta_{e\infty} < \sqrt{\frac{m_e}{m_i}} \quad . \quad (4)$$

At the full mass ratio $m_i/m_e = 1836$ this condition is $\beta_{e\infty} < 0.02$, whereas for $m_i/m_e = 400$ (applied in our simulations) the derived threshold is $\beta_{e\infty} < 0.05$. Again, the simulation studied here is for a value $\beta_{e\infty} = 0.003$, and indeed, at later times in the run strong non-adiabatic behavior is observed, resulting in values of p_{\parallel} and $e\Phi_{\parallel}/T_{e\infty}$ much larger than those predicted by the adiabatic theory.

B. Electron holes, double layers and the formation of a large amplitude acceleration potential

As mentioned above, the acceleration potential with $e\Phi_{\parallel}/T_{e\infty} \simeq 18$ in Fig. 1(b) recorded for $t\Omega_{ci} = 31$ is consistent with the scaling law for Φ_{\parallel} in Eq. (2). In contrast, the acceleration potential for $t\Omega_{ci} = 56$ displayed in Fig. 2(c) has a much larger magnitude, $e\Phi_{\parallel}/T_{e\infty} \simeq 100$, and is caused by the formation of structures in E_{\parallel} for which the largest amplitudes are observed within density cavities. The associated jumps in Φ_{\parallel} are consistent with double layers [9–11]. The existence of such electron holes and double layers is well documented by spacecraft observations within the magnetosphere. In the early observations they were termed *broadband electrostatic noise* [24] but Geotail observations showed they are solitons and not monochromatic mixture or coherent broadband tones [25]. More modern and detailed observations include events recorded by the THEMIS mission [26, 27] and the Van Allen probes [28].

Two density cavities (with strong double layers) are clearly seen near the separators in Fig. 2(a) for $x/d_i \simeq 200$. In Fig. 2(c) four points, $d - g$, are selected on a field line sampling the center of a large amplitude structure in Φ_{\parallel} . The corresponding distributions are shown in Figs. 2(d–g). For point d the value of $e\Phi_{\parallel}/T_{e\infty} \simeq 5$ is relatively small; the distribution mainly consists of a

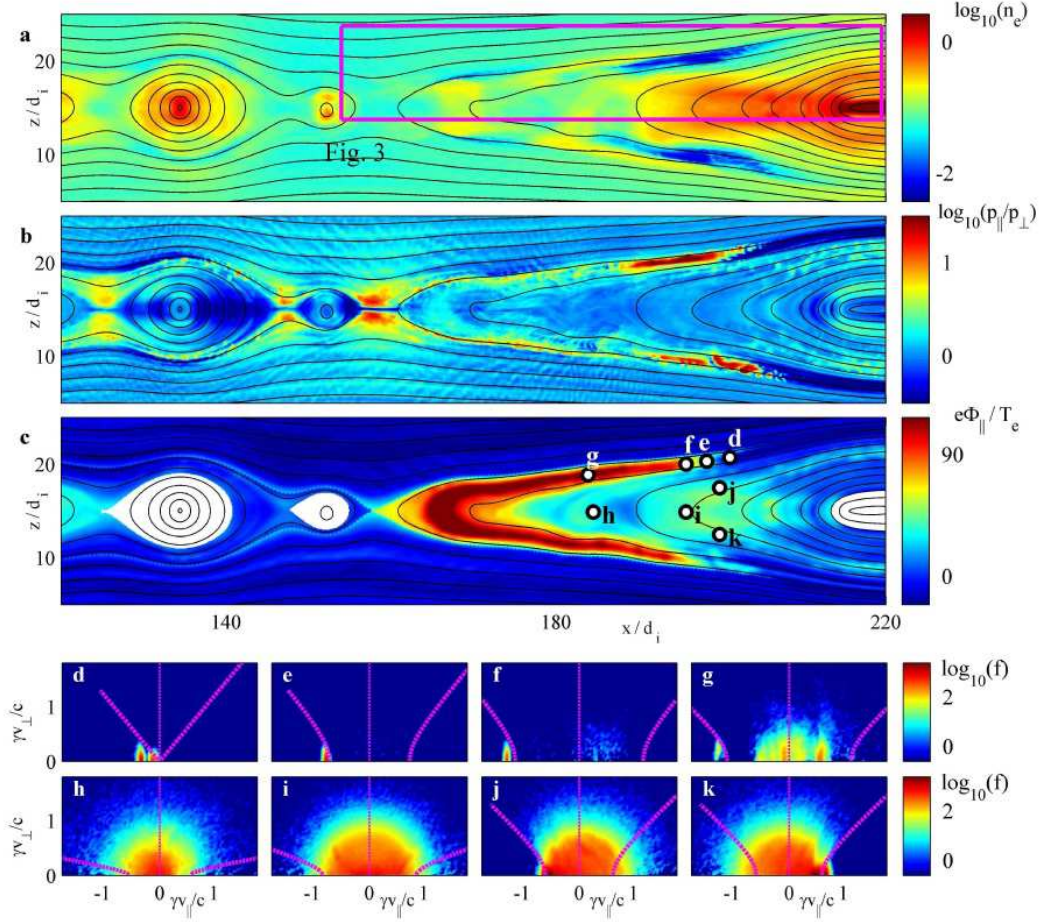


FIG. 2: (a-c): Color contours of constant density $\log_{10}(n_e)$, pressure anisotropy $\log_{10}(p_{\parallel}/p_{\perp})$, and acceleration potential $e\Phi_{\parallel}/T_e$. Spatial locations are marked in (c) for which $f(v_{\parallel}, v_{\perp})$ is shown in panels (d) to (k). The magenta lines in (d) to (k) mark the trapped-passing boundaries as defined by Eq. (13).

beam of incoming electrons. Likewise for points e and f , the distributions are almost purely composed of the incoming beams energized by Φ_{\parallel} with velocities reaching $\gamma v_{\parallel}/c \simeq -1.2$. For point g , in addition to the incoming beam, a population of electrons are observed mostly with velocities $\gamma v/c < 0.7$. These relatively hot electrons originate from the reconnection region, but given the large amplitude of Φ_{\parallel} , they are deeply trapped and cannot escape the reconnection region by parallel streaming along field lines.

To provide more details on these large scale structures yielding direct acceleration of the incoming electrons, in Fig. 3(a) a zoom-in-view is given for the region outlined in Fig. 2(a). Within this region seven field lines are selected for which $f_{\parallel}(\mathbf{x}, v_{\parallel}) = 2\pi \int v_{\perp} f dv_{\perp}$ are computed. The resulting $f_{\parallel}(\mathbf{x}, v_{\parallel})$ are displayed in Figs. 3(b-h) as functions of x along the selected field lines. The upper most field line (b) in Fig. 3(a) is just upstream of the density cavities. The corresponding f_{\parallel} along this field line is shown in Fig. 3(b). Signatures of developing instabilities are seen for $x/d_i \simeq 170$.

Strong instabilities are visible along the second field line (c) for which f_{\parallel} displays evidence of both electron holes and double layers. The electrons with $\gamma v_{\parallel} > 0$ are streaming away from the reconnection region. The first double layer for $x/d_i \simeq 170$ is seen to help confine elec-

trons energized in the X-line region. However, the second double layer at $x/d_i \simeq 200$ develops without the presence of energized electrons from the reconnection site.

Figs. 3(d,e) illustrate how the double layers continue to develop. The vertical magenta lines marked $d - g$ in Fig. 3(e) correspond to the distributions in Figs. 2(d-g), respectively. The beams in Figs. 2(d-g) are readily identified as the structure (with $\gamma v_{\parallel} < 0$) in f_{\parallel} containing incoming electrons continuously accelerated by Φ_{\parallel} . For these field lines at the center of the density cavity, $e\Phi_{\parallel}$ is larger than the energies of electrons streaming away from the reconnection site. Thus, for $x/d_i > 200$ almost no escaping electrons (electrons with $\gamma v_{\parallel} > 0$) are observed.

The magnitude of the double layer in Fig. 3(f) is still large. In addition to the incoming beam, the double layer is now being filled with energetic electrons streaming away from the reconnection site and reflected back again by the double layer. Considering the evolution of f_{\parallel} in Figs. 3(b-f) it is clear that the acceleration by Φ_{\parallel} of the incoming electron beam and the subsequent mixing in electron holes is responsible for the main heating of the electrons on these field lines intersecting the density cavities.

Deeper into the exhaust the value of Φ_{\parallel} is reduced. This is evident in Figs. 3(g,h) where the incoming electron beam now has velocities on the order of $\gamma v_{\parallel}/c \simeq$

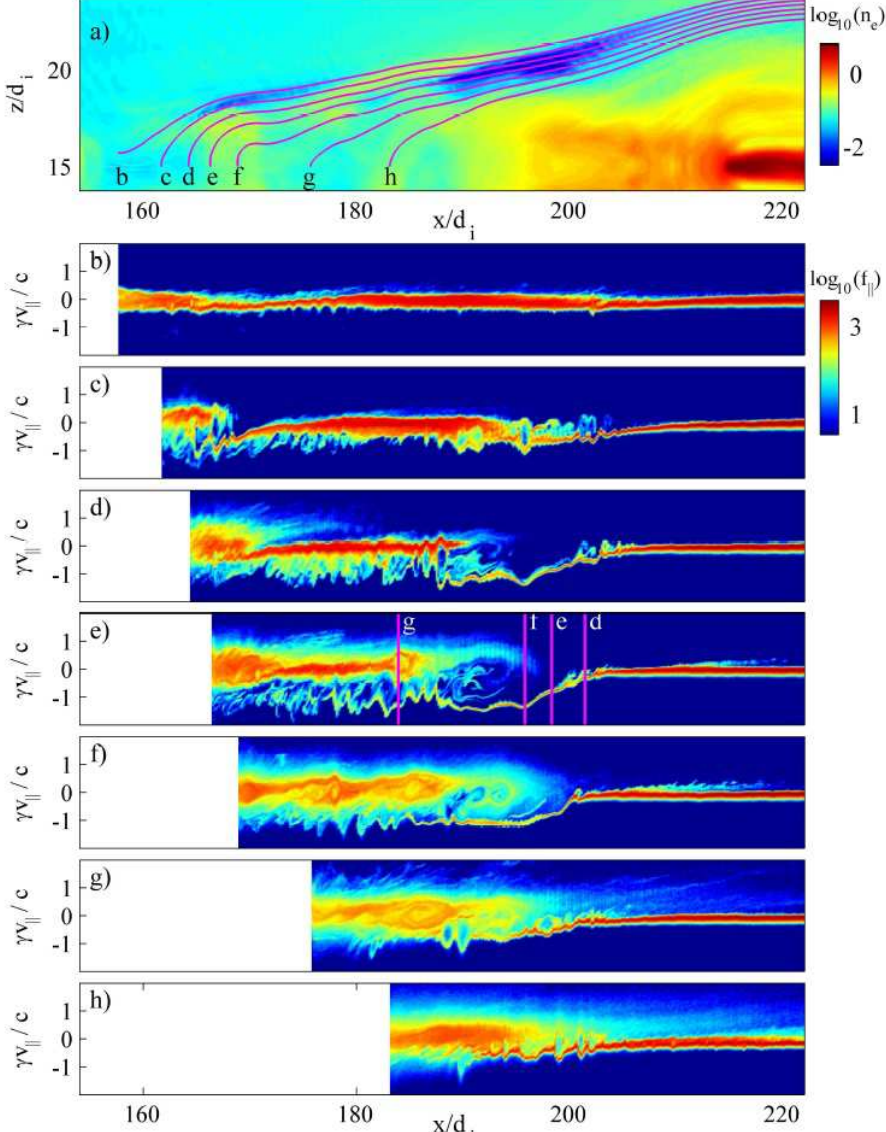


FIG. 3: a) Color contours of constant density, $\log_{10}(n_e)$. Strong density cavities are observed where the density is reduced by a factor of 10 below the upstream value. Seven field lines are selected and marked *b* to *h*. Along each field line the parallel distribution is computed, $f_{\parallel}(v_{\parallel}) = 2\pi \int f v_{\perp} dv_{\perp}$, and displayed in panels *b*) to *h*) as functions of γv_{\parallel} and x/d_i . The magenta lines in *e*) marked *d*–*g* indicate the positions corresponding to the distributions in Fig. 2(*d*–*f*), respectively.

–0.8. The reduced values of Φ_{\parallel} allow energized electrons to escape the reconnection region and finite values of f_{\parallel} are thus observed for $x/d_i > 200$ with $\gamma v_{\parallel} > 0$. These escaping electrons carry a significant heat flux away from the reconnection region.

C. Formation of strong double layers

Recently, Li *et al.* [16, 29, 30] investigated the formation of double layers at the interface between hot electrons energized at the reconnection site and cold electrons streaming into the reconnection region along field lines. Their numerical studies document electron holes and double layers with signatures similar to those observed in our simulations outside the density cavities (i.e. in Figs. 3(*g*,*h*)). They modelled the hot electrons from the reconnection region as a Maxwellian with a temperature T_h and observed double layer amplitudes, $e\Phi_{\text{DL}} \simeq 0.73T_h$, less than T_h . This moderate amplitude

allows for a significant fraction of the energetic electrons to escape [16].

Interestingly, the strong double layers that form within the density cavities in Figs. 3(*c*–*f*) appear to have some characteristics different from those studied by Li *et al.*. For example, we here observe an amplitude much larger than the energy of electrons energized at the reconnection site, allowing no electrons to escape by parallel streaming along field lines. Furthermore, the development of these large amplitude double layers is not driven by hot electrons streaming away from the reconnection region. This is clear because the strong double layer structure at $x/d_i \simeq 200$ in Figs. 3(*c*–*d*)) develops before energetic electrons from the reconnection region reach this location (about $40 d_i$ downstream of the x-line). Below we argue that the strong double layers (distinct from the double layers outside the density cavities) form not just to reduce free streaming losses, but primarily to boost the electron density within the reconnection region.

From the principle of quasi-neutrality, electric fields in

a plasma develop to maintain near equal densities of electrons and ions. To elucidate the mechanisms driving the strong double layers, in Fig. 4(a) contours of the parallel electron flux are shown for the reconnection region, and large fluxes of electrons $|n_e u_{e\parallel}|/n_\infty v_{te\infty} \simeq 4$ flow toward the reconnection region. Thus, this flow is stronger than the incoming parallel flux of upstream electrons $\Gamma_{\parallel\infty} = 2\pi \int_0^\infty dv_\parallel \int_0^\infty v_\perp dv_\perp v_\parallel f_\infty = n_\infty v_{te\infty}/(2\sqrt{\pi})$.

To understand why the parallel flux of electrons is needed, we consider the blue area, $A_1 (= L dl)$ on the schematic flux-tube in Fig. 4(b). During the reconnection process this area convects into the larger green area A_2 . From magnetic flux conservation within the flux-tube, the areas of the blue and green regions are related as

$$A_2 = A_1 \frac{B_1}{B_2} ,$$

where B_1 and B_2 are representative magnetic field strengths within the two areas. As the in-plane magnetic field vanishes at the X-line, as is ubiquitous in reconnection we have $B_1 > B_2$. The areas considered are within the ion diffusion region where the ions are decoupled from the magnetic field lines. The simulation shows that within this region the ion density, n , is nearly uniform, such that area A_2 includes an increased number of ions compared to area A_1 . This increase can be estimated as

$$\Delta N = n(A_2 - A_1) = nL dl \left(\frac{B_1}{B_2} - 1 \right) . \quad (5)$$

Meanwhile, the electrons are *frozen in* to the magnetic field in their perpendicular motion, so the matching increase ΔN of electrons (required for quasi neutrality) must be supplied by a parallel electron flux $n_e u_{e\parallel}$.

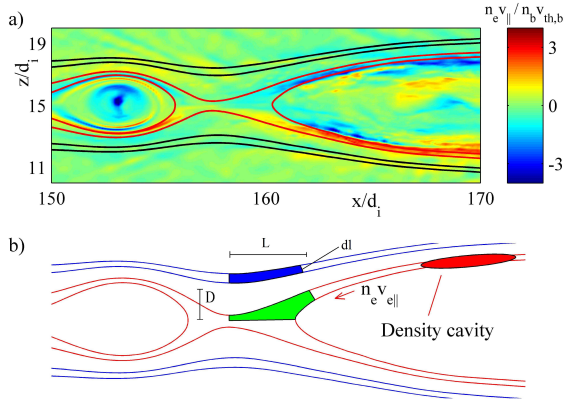


FIG. 4: a) Contours of parallel electron flows into the reconnection region. b) Schematic illustration of a flux tube section (blue) expanding as it enters the reconnection region (green). To maintain a uniform electron density (required for quasi neutrality) electrons flow along field lines into the green region driving the formation of the density cavity marked in red.

To estimate $u_{e\parallel}$ we consider again the characteristic length scales D and L across and along the reconnection region. Previous studies (including Ref. [31]) have established that the inflow velocity upstream of the ion diffusion region is $(D/L)v_A$, with $D/L \simeq 0.1$. Meanwhile, inside the ion diffusion region the velocity of the flux-tubes are enhanced by the factor B_1/B_2 yielding $v_{in,e} = v_A B_1 D / (L B_2)$. Thus, region A_1 with length L convects into region A_2 during a time $\tau \simeq D/v_{in,e} = L B_2 / (v_A B_1)$. The increase in the number of electrons within the considered area can then be estimated as $\Delta N = n u_{e\parallel} dl \tau$. Equating this with Eq. (5) the factors of n , L and dl cancel such that

$$u_{e\parallel} = v_A \frac{B_1}{B_2} \left(\frac{B_1}{B_2} - 1 \right) \simeq 4v_A ,$$

where we have assumed a ratio $B_1/B_2 \simeq 2.5$. This result may be rewritten on the form

$$\frac{u_{e\parallel}}{v_{te\infty}} = 4 \sqrt{\frac{m_e}{m_i}} \frac{1}{\sqrt{\beta_{e\infty}}} , \quad (6)$$

so for the present simulation (and in agreement with Fig. 4(a)) we then obtain $u_{e\parallel} \simeq 4v_{te\infty}$.

In kinetic and also Hall MHD simulations of reconnection at larger values of $\beta_{e\infty}$ less pronounced density cavities are typical along the separators, and it has been argued that they develop to maintain pressure balance perpendicular to separators [32]. We here emphasize the role of electrons streaming into the reconnection region as the more important cause for the near depletion of electrons from the density cavities. To the best of our knowledge, this additional mechanism for density depletion is described here for the first time. We also note that the resulting pattern of the parallel electron currents along the separators are largely responsible for the characteristic Hall magnetic field of the reconnection region [33].

The development of the observed strong double layers is likely to be suppressed when $n_\infty u_{e\parallel} < \Gamma_{\parallel\infty} = n_\infty v_{te\infty}/(2\sqrt{\pi})$, allowing thermal streaming of electrons to supply the reconnection region with the electrons needed. With Eq. (6), a crude criteria for the development of the strong double layers is then

$$\beta_{e\infty} \lesssim 200 \frac{m_e}{m_i} . \quad (7)$$

For $m_i/m_e = 400$ this criteria suggests that the strong double layers may already form at $\beta_{e\infty} < 0.5$. However, the derivation of Eq. (7) does not include the effects of the adiabatic Φ_\parallel given in Eq. (1) helping to boost the electron flow into the reconnection region. In contrast, the condition in Eq. (4) includes the flows driven by Φ_\parallel and therefore provides a more accurate threshold for the transition to the non-adiabatic parallel dynamics. Nevertheless, we include the above derivation of Eq. (7) as it elucidates the mechanisms we believe are important for the formation of the density cavities and the associated strong double layer formation.

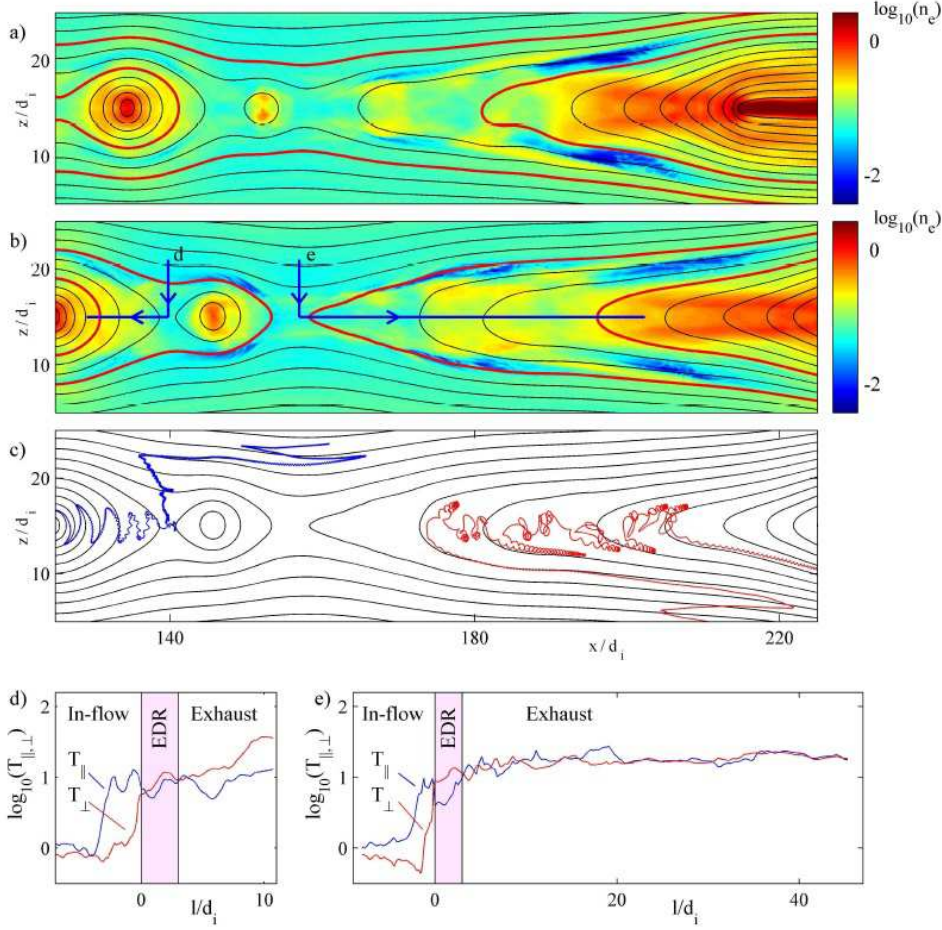


FIG. 5: a,b): Contours of constant density for $t\Omega_{ci} = 56$ and $t\Omega_{ci} = 61$, respectively. c) Typical electron test orbits trajectories. In the left side exhaust the electron magnetic moments are conserved, whereas the chaotic electron motion in the right side exhaust is non-adiabatic. d,e): Electron temperature components evaluated along the lines shown in b).

III. PROPERTIES OF THE PITCH ANGLE MIXED EXHAUST

A. Signatures of the pitch angle mixed exhaust

The dynamics in the right side exhaust (for $x/d_i > 160$) in Fig. 2 are different from the left side not only because of the asymmetry in Φ_{\parallel} . Another main difference is that within the right side exhaust the magnetic moments of the electrons are not conserved when the electrons cross the mid-plane. The distributions for the points marked $h - k$ in Fig. 2(c) are shown in Figs. 2(h-k). The points h and i are both at the mid-plane and we notice how their distributions are independent of the pitch angle $\theta = \angle(\mathbf{v}, \mathbf{B})$. This is the signature of complete pitch angle mixing.

The magnetic moment, $\mu = mv_{\perp}^2/2$, is only an adiabatic invariant of the electron motion when the radius of curvature of the magnetic field R_c is larger than the electron Larmor radius $\rho_l = mv_{\perp}/(eB)$. This requirement for adiabatic motion may also be expressed as $\kappa^2 = R_c/\rho_l > 1$ along the full electron trajectory [34]. In the center of the exhaust the strongly bent field lines in combination with the low magnetic field strength, can lead to non-adiabatic electron motion with $\kappa^2 < 1$. This causes electrons to pitch angle mix, washing out

anisotropic structures in velocity space.

To further explore the temporal evolution of the plasma, in Figs. 5(a,b) density profiles for $t\Omega_{ci} = 56$ and $t\Omega_{ci} = 61$ are given, respectively. The main density cavities of $t\Omega_{ci} = 56$ are seen to move downstream with the exhaust while new cavities form closer to the x-line. During this downstream propagation the cavities remain characterized by large values of E_{\parallel} , such that the region of parallel energization is expanding in time.

Examples of test particle orbits are given in Fig. 5(c). For the part of the blue trajectory which falls within the left side exhaust, the magnetic moment is an adiabatic invariant. Meanwhile, for the red trajectory typical of the right side exhaust, the magnetic moment is not conserved where the particles pass through the midplane of the domain.

The described particle motion has direct implications on the pressure profiles. This is evident in Figs. 5(d,e) where the parallel and perpendicular pressure components are evaluated along the lines marked d and e in Fig. 5(b). Consistent with the EOS by Le *et al.* for both inflow regions we observed $T_{e\parallel} \gg T_{e\perp}$. At the end of the electron diffusion regions pitch angle mixing leads to $T_{e\parallel} = T_{e\perp}$. For the left side, the magnetic islands lead to an increase of the field strength in the exhaust such that the magnetic moments of the electrons are conserved, and

the betatron heating is effective. This leads to the temperature components with $T_{e\perp} > T_{e\parallel}$, and is in contrast to the right side exhaust where pitch angle mixing yields $T_{e\perp} \simeq T_{e\parallel}$.

B. Simulation profiles of the pitch angled mixed exhaust

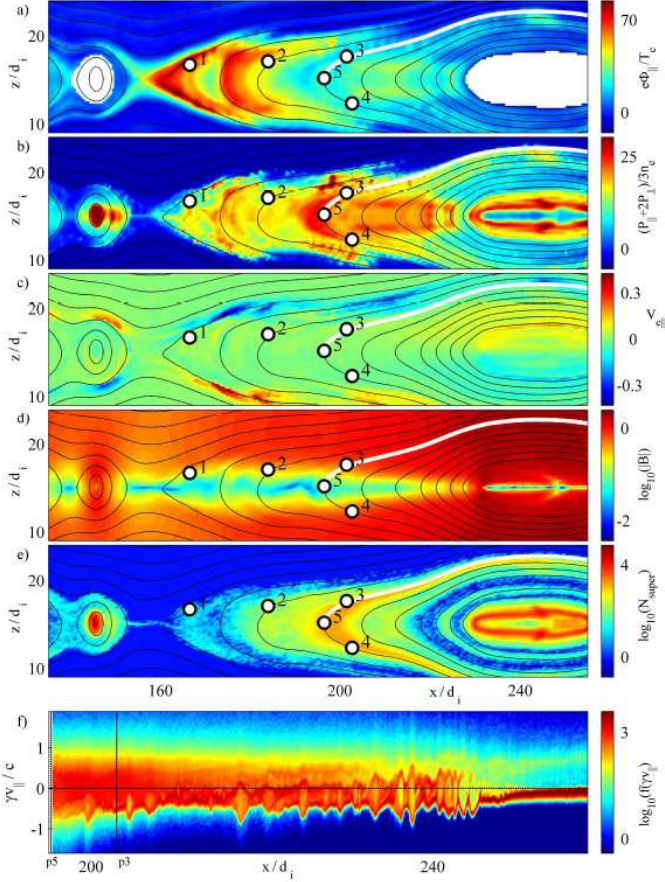


FIG. 6: Kinetic simulation results showing contours of a) $e\Phi_{||}/T_e$, b) $T_e = \text{Tr}(\mathbf{P}_e)/3n_e$, c) $V_{e||}$, d) $\log_{10}(B)$, and e) n_{super}/n representing the density of electrons with $\gamma v/c > 2.5$. f) parallel phase-space distribution $f_{||}(\gamma v_{||})$ as a function of x along the field-line highlighted in white in (a)-(e). The simulation results shown correspond to time $t\Omega_{ci} = 61$.

Key profiles for the electron dynamics at $t\Omega_{ci} = 61$ are given in Fig. 6. The area of a significant acceleration potential ($e\Phi_{||}/T_{e\infty} > 30$) in Fig. 6(a) is much larger than at previous time, $t\Omega_{ci} = 56$, considered in Fig. 2(c). In the right side exhaust, the boundaries for large values of $e\Phi_{||}/T_{e\infty} (> 30)$ coincide with the boundaries where the effective electron temperature, $T_e = (p_{||} + 2p_{\perp})/3n_e$, in Fig. 6(b), displays an abrupt increase (by about a factor of 20) from its value in the inflow. This is consistent with our conclusions above that the $E_{||}$ of the electron holes and double layers provides strong energization of

the incoming electrons. This parallel heating is most significant within the density cavities, which, as displayed in Fig. 6(c), are characterized by the strongest streaming of electrons directed towards the reconnection region.

As discussed above, due to the low values of B observed in Fig. 6(d) along the exhaust mid-plane, the electron motion in the right side exhaust is non-adiabatic. Although the pitch angle mixing is limited to this region of low B , due to the non-localized motion of the trapped electrons, the pitch angle mixing impacts the electron distributions in the full width of the exhaust. We also note, that in contrast to the bulk electron heating, the generation of superthermal electrons occurs gradually in the exhaust. This is evident in Fig. 6(e) where density contours are given for superthermal electrons with $\gamma v/c > 2.5$.

The parallel electron dynamics along a typical exhaust field line is illustrated in Fig. 6(f). As in Fig. 3, the contours represent constant values of $f_{||}(v_{||}) = 2\pi \int f v_{\perp} dv_{\perp}$, here as a function of x along the field line highlighted in white in Figs. 6(a-e). Again, large electron hole structures are observed, especially at the interface (for $x/d_i \simeq 240$) between the cold incoming electrons and electrons already heated in the exhaust.

C. Relative importance of $E_{||}$ and E_{\perp} for electron energization in the pitch angle mixed exhaust

It is interesting to explore the relative importance of parallel and perpendicular electric fields for energizing the exhaust electrons. The local energy gain of the electron fluid is quantified by $\mathbf{E} \cdot \mathbf{J}_e$. As shown in Fig. 7(a) we divide a part of the simulation domain into sectors of equal increments in the in-plane magnetic flux, A_y . The energy exchange terms $E_{||}J_{e||}$, $\mathbf{E} \cdot \mathbf{J}_e$, and $\mathbf{E} \cdot \mathbf{J}_i$ are integrated over each sector and displayed in Fig. 7(b). Within the sector including the separator and the following two downstream sectors, $E_{||}J_{e||}$ amounts to about 50% of the total $\mathbf{E} \cdot \mathbf{J}_e$. As shown in Fig. 6(e), these sectors include regions of strong electron flows $V_{e||}$ toward the X-line. Because $\Phi_{||}$ is generally increasing as the X-line is approached, incoming electrons are energized by $E_{||}$.

Further downstream of the X-line the electron flow is away from the X-line (see Fig. 6(c)), such that the electrons endure a net loss of energy through work against $E_{||}$. In fact, the average value of $E_{||}J_{e||}$ in the exhaust is small, while the heating by $\mathbf{E}_{\perp} \cdot \mathbf{J}_{e\perp}$ accounts for nearly all the electron energization when integrated over the exhaust. Also noteworthy, as can be seen in the traces in Fig. 7(b) the electrons acquire about 20% of the total dissipated magnetic energy, which is large compared to levels typically observed in simulations at higher $\beta_{e\infty}$.

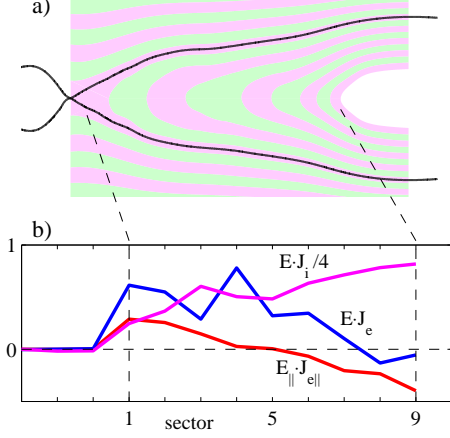


FIG. 7: a) The cross-section is sectorized into intervals of A_y . For each sector $E_{\parallel}J_{e\parallel}$, $\mathbf{E} \cdot \mathbf{J}_e$, and $\mathbf{E} \cdot \mathbf{J}_i$, is evaluated as displayed in b).

D. Rate of electron energization by the reconnection electric field

It is natural to suspect the reconnection electric field, E_{rec} , to be the cause of the documented energization by \mathbf{E}_{\perp} . The rate of this energization is given by $P = E_{\text{rec}}J_{ey}$, where J_{ey} is the electron current in the y -direction. The strongly curved field lines of the exhaust are favorable for energization related to the curvature drift [35]. This is shown directly in appendix A where we apply the guiding center model and obtain a Fermi-like energization rate proportional to the particle energy. However, it is not obvious that the guiding center model is applicable to the present exhaust where the magnetic moments of the electrons are not conserved. This motivates a more general derivation of the heating rate without the assumption of adiabatic electron motion. Therefore, we will estimate the heating rate using a more general formulation. This estimate will also include the possible contributions from the magnetization currents (normally neglected in calculations based on the guiding center model [35]). The end result is the confirmation of the heating rates obtained with the guiding center model.

Our generally valid approach for estimating the heating rate of electrons in the pitch angle mixed exhaust is first to generalize the MHD-force balance equation, $\mathbf{J}_{\delta} \times \mathbf{B}_{\delta} = \nabla p_{\delta}$, where the subscript δ denotes a particular class of electrons with $v \simeq v_0$ for $t = t_0$. We may thereby determine $J_{\delta y}$ as a function of the electron energy, which in turn will provide us with the energization rate due to the reconnection electric field as a function of energy.

To limit the analysis to electrons with an initial velocity around v_0 at time t_0 , we introduce $f_{\delta}(\mathbf{x}, \mathbf{v}, t)$ which

at $t = t_0$ is given by

$$f_{\delta}(\mathbf{x}, \mathbf{v}, t) = \begin{cases} f(\mathbf{x}, \mathbf{v}, t) & , \quad v_0 - \delta v < |\mathbf{v}| < v_0 + \delta v \\ 0 & , \quad \text{elsewhere} \end{cases} \quad (8)$$

Naturally, the time evolution f_{δ} is governed by the Vlasov equation

$$\frac{\partial f_{\delta}}{\partial t} + \mathbf{v} \cdot \nabla_{\mathbf{x}} f_{\delta} - \frac{e}{m_e} (\mathbf{E} + \mathbf{v} \times \mathbf{B}) \cdot \nabla_{\mathbf{v}} f_{\delta} = 0 \quad , \quad (9)$$

and moments over f_{δ} are defined in the regular fashion as

$$\langle \mathbf{v}^l \rangle_{\delta} = \int \mathbf{v}^l f_{\delta} d^3v \quad ,$$

yielding n_{δ} , $n_{\delta} \mathbf{u}_{\delta}$ and \mathbf{P}_{δ} for $l = 0, 1$, and 2 , respectively.

In analogy with the derivation of the standard electron momentum equation, by taking the $l = 1$ -moment (or the \mathbf{v} -moment) of Eq. (9) we obtain a momentum equation for the selected electrons

$$m_e n_{\delta} \frac{d\mathbf{u}_{\delta}}{dt} = -en_{\delta}(\mathbf{E} + \mathbf{u}_{\delta} \times \mathbf{B}) - \nabla p_{\delta} - \nabla \cdot \pi_{\delta} \quad .$$

Here we have split the pressure tensor, \mathbf{P}_{δ} , into its scalar part $p_{\delta} \mathbf{I}$ and the shear stress π_{δ} . For the pitch angle mixed exhaust, the latter is assumed to be negligible, $\pi_{\delta} \simeq 0$. For $t = t_0$, all electrons contributing to p_{δ} have velocities $v \simeq v_0$ and we thus find $p_{\delta} = (2m_e/3)n_{\delta}v_0^2 = (4/3)n_{\delta}\mathcal{E}_0$, with $\mathcal{E}_0 = m_e v_0^2/2$.

Our aim is next to derive an expression for the average electron drift in excess of the $\mathbf{E} \times \mathbf{B}$ -drift. We therefore introduce $\mathbf{u}_{D\delta} = \mathbf{u}_{\delta} - \mathbf{E} \times \mathbf{B}/B^2$. Neglecting inertia, $m \rightarrow 0$, we obtain the following momentum equation for electrons within the considered velocity interval:

$$0 = -en_{\delta}(\mathbf{E}_{\parallel} + \mathbf{u}_{D\delta} \times \mathbf{B}) - \frac{4\mathcal{E}_0}{3} \nabla n_{\delta} \quad .$$

The current density carried by these electrons is $\mathbf{J}_{\delta} = -en_{\delta}\mathbf{u}_{D\delta}$ and the momentum balance perpendicular to the magnetic field is then governed by

$$\mathbf{J}_{\delta} \times \mathbf{B} = \frac{4\mathcal{E}_0}{3} \nabla_{\perp} n_{\delta} \quad . \quad (10)$$

An approximate heating rate is readily obtained from the above equation. The average z component of the left hand side may be estimated as

$$(\mathbf{J}_{\delta} \times \mathbf{B})_z \simeq \langle J_{\delta y} \rangle \langle B \rangle \quad , \quad (11)$$

where $\langle \dots \rangle$ denotes an average over the z -direction. Furthermore, to estimate the right hand side of Eq. (10) we write $\nabla n_{\delta} \simeq n_{\delta}/D$ such that Eq. (10) approximately yields

$$\frac{\langle J_{\delta y} \rangle}{n_{\delta}} \simeq \frac{4}{3} \frac{\mathcal{E}_0}{D \langle B \rangle} \quad .$$

Next, with $E_{\text{rec}} \simeq v_A \langle B \rangle$ we obtain the following result for the heating rate

$$\frac{d\mathcal{E}}{dt} = \frac{\langle J_{\delta y} \rangle E_{\text{rec}}}{n_{\delta}} \simeq \frac{4\mathcal{E}_0 v_A}{3D} .$$

A comparison with the simulation shows that this expression overpredicts the heating rate by about a factor of two. However, using the numerical profiles to improve the various estimations above (such as $\nabla n_{\delta} \simeq n_{\delta}/D$ and Eq. (11)) we obtain our final expression for the heating rate consistent with the simulation

$$\frac{d\mathcal{E}}{dt} \simeq \mathcal{E}_0 \frac{v_A}{2D} . \quad (12)$$

Accordingly, electrons trapped in the exhaust double their energy during an Alfvénic transit time across the full width of the exhaust, $2D$.

The energization rate in Eq. (12) is proportional to the initial energy of the electrons, and is similar to the rate for electrons in contracting magnetic islands [3]. This magnetic island model was introduced to allow for energization in extended reconnection exhausts filled with a bath of magnetic islands. Meanwhile, according to Eq. (12) electron energization in the reconnection exhaust is effective even without magnetic islands and is not contingent on the development of pressure anisotropy (the latter has been found essential for energization by magnetic island [6]). In our analysis, the only requirement for electron energization is that electrons are confined to the reconnection exhaust, which here is aided by the strong Φ_{\parallel} associated with the double layer formation.

We further note that for a magnetized exhaust, our starting point in Eq. (10) can be derived directly by integrating the current carried by the guiding center drifts \mathbf{v}_D and magnetization current $\mathbf{J}_{e\perp} = e \int \mathbf{v}_D f d^3v + \nabla \times \mathbf{M}$, with the magnetization $e\mathbf{M} = \mathbf{b} \int \mu f d^3v$. Thus, the present analysis is therefore consistent with similar findings obtained using the guiding center model [36]. In fact, in Appendix A we show that Eq. (12) is readily derived using the guiding center model.

IV. FLAT-TOP DISTRIBUTIONS AND SUPERHERMAL ELECTRON ENERGIZATION

In this Section we explore the heating of electrons in the exhaust. A statistical model is derived which characterizes the energy distribution of the superthermal electrons. While these electrons are mainly energized by perpendicular electric fields, we document how the initial energization and confinement provided by Φ_{\parallel} significantly enhances the effectiveness of the electron energization process.

A. The trapped passing boundaries

In Figs. 8(a,b) we consider different classes of electron trajectories reaching the points highlighted. The trajectories

passing through the reconnection region along field lines without any reflections are marked by A and D , and we denote these as passing. Meanwhile the trajectories marked B and C we denoted as trapped, with electrons bouncing back and forth along field lines, as the field lines convect across the reconnection region. The four classes of trajectories divide the $(v_{\parallel}, v_{\perp})$ -plane as shown in Fig. 8(c). The trajectories of velocity regions A and B reach the point considered with a negative value of v_{\parallel} , whereas $v_{\parallel} > 0$ for trajectories of regions C and D . The boundary between regions A and B and the boundary between regions C and D we denote the trapped/passing boundaries. In Fig. 8(c) these are shown by the magenta lines.

When the magnetic moment is conserved the perpendicular energy is given by $\mathcal{E}_{\perp} = \mu B$, implying that the parallel energy is $\mathcal{E}_{\parallel} = \mathcal{E} - \mu B_{\infty}$. It then follows that the trapped/passing boundaries are found by solving the equation

$$\mathcal{E}_{\parallel\infty} = \mathcal{E} - e\Phi_{\parallel} - \mu B_{\infty} = 0 , \quad (13)$$

which expresses the physical condition that marginally trapped electrons will deplete their parallel energy ($\mathcal{E}_{\parallel\infty} = 0$) as they barely escape along the magnetic field lines away from the reconnection region. We note that for $v_{\perp} = 0$ the trapped/passing boundaries start at $|v_{\parallel}| = v_{\phi} = \sqrt{2e\Phi_{\parallel}/m_e}$ and at large v they asymptote to the line in Fig. 8(c) characterized by the angle α , with $\cos(\alpha) = B/B_{\infty}$.

B. Size of the loss-cone in velocity space

For the analysis below it is convenient to introduce R_{loss} as a measure of the size of the electron loss-cones, where $4\pi R_{\text{loss}}$ is the solid angle in velocity space of the loss-cones. Using the expression for the trapped/passing boundary in Eq. (13) it is readily shown that

$$R_{\text{loss}} = 1 - \left[1 - \frac{B}{B_{\infty}} \left(1 - \frac{e\Phi_{\parallel}}{\mathcal{E}} \right) \right]^{1/2} .$$

Introducing the characteristic velocity of the acceleration potential $v_{\phi} = \sqrt{2e\Phi_{\parallel}/m_e}$, an approximate form is obtained for the limit $B \ll B_0$

$$R_{\text{loss}} \simeq \frac{B}{2B_{\infty}} \left(1 - \frac{v_{\phi}^2}{v^2} \right) , \quad (14)$$

valid for $|\mathbf{v}| > v_{\phi}$. For $|\mathbf{v}| < v_{\phi}$ the confinement is absolute with $R_{\text{loss}} = 0$.

C. Generation of flattop distributions in the pitch angle mixed exhaust

The bulk exhaust distributions for the time slice of Fig. 6 are displayed in Figs. 9. First, consider the distribution in Fig. 9(a) corresponding to the point marked

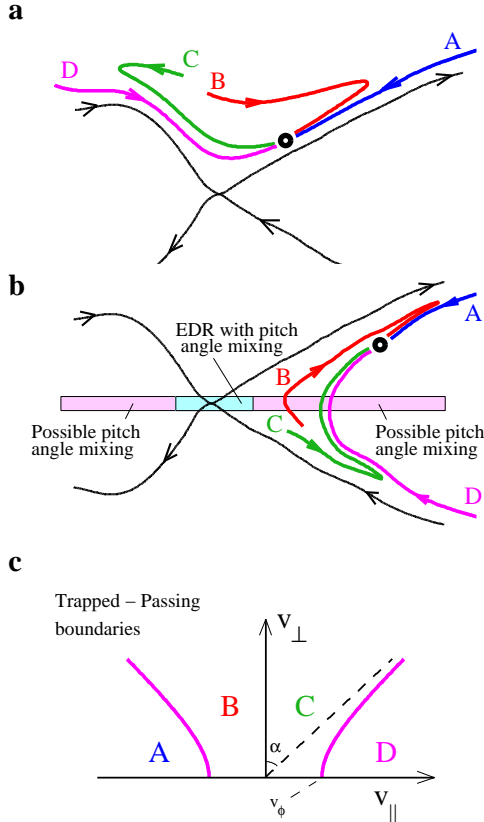


FIG. 8: a) Classification of electron trajectories reaching a point in the inflow region. Trajectories A and D are passing while trajectories B and C are trapped. b) Similarly to the inflow region, the trajectories in the exhaust can be classified as passing and trapped. In the exhaust of antiparallel reconnection, pitch angle mixing always occurs at the end of the electron diffusion region. In some cases, pitch angle mixing remains effective far downstream of the reconnection site. c), Regions in the $(v_{\parallel}, v_{\perp})$ -plane identifying the velocity regions of the four classes of electron trajectories. The magenta lines represent the trapped/passing boundaries of Eq. (13).

“3” in the panels of Fig. 6. As above, the velocity space (spanned by γv_{\parallel} and γv_{\perp}) is divided into regions A, B, C, and D with distinct properties of the associated electron trajectories classified in Fig. 8. Again, the trapped/passing boundaries between regions A/B, and regions C/D, are computed using Eq. (13). Trajectories of velocity region A are incoming electrons streaming along field-lines toward the reconnection layer. The electrons in velocity region C and D are all streaming away from the X-line, but the electrons in region C are trapped and will reflect into region B. Meanwhile, the electrons in region D have sufficient parallel energy to escape and will exit the simulation domain at the open boundaries.

The changes in the Fig. 9(a) distribution are dramatic across the A/B boundary calculated using Eq. (13). The region A electrons are well characterized as beams with a parallel energy $e\Phi_{\parallel}$. A small spread is observed about the center of the beams corresponding to the low up-

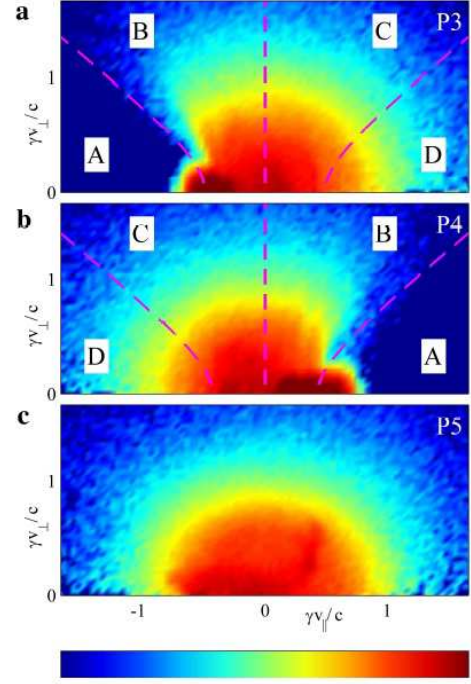


FIG. 9: Color contours of the electron distribution function for the points marked P3, P4 and P5 in Fig. 6. For the distributions at P3 and P4 the velocity regions A to D correspond to the distinct trajectories shown in Fig. 7(a) and described in the text. Because of the low values of the magnetic field in the center of the exhaust, pitch angle mixing is effective and the P5 distribution is fully isotropic. For energies $\mathcal{E} < e\Phi_{\parallel}$ the values of f are nearly constant, resembling flattop distribution observed *in situ* in the magnetotail.

stream temperature of these incoming electrons. The distribution in Fig. 9(b) is for the point below the midplane marked “4” in the panels of Fig. 6. Given the chances in direction of B_x , we note how these beams of incoming electrons have opposite signs of γv_{\parallel} above and below the mid-plane.

The region A beams terminate at the midplane of the simulation domain where, as shown in Fig. 6(d), the magnetic field is weak, $B/B_0 < 0.1$. This is also evident in the distribution in Fig. 9(c) corresponding to the point marked “5” in Fig. 6 on the same field-line as points 3 and 4. The weak magnetic fields causes a complete breakdown of the magnetic moment as an adiabatic invariant and the resulting chaotic electron motion causes the distributions within this layer to become fully isotropic in velocity space.

As the isotropized electrons of velocity region A leave the midplane they populate velocity regions B, C and D throughout the exhaust. In principle, these electrons should only add to f at their injection energy $\mathcal{E} = e\Phi_{\parallel}$. However, distributions in velocity space with negative slope ($df/dv < 0$) are unstable and instabilities (including electrons holes) develop in the simulation which are responsible for scattering of the electron en-

ergies. These processes and the energization mechanism described by Eq. (12) drive the distribution function towards $df/dv \simeq 0$, such that for $\mathcal{E} \leq e\Phi_{\parallel}$ flat-top distributions are approached where $f \simeq \text{const}$ [14, 37, 38].

D. Statistical model for superthermal electrons

We now seek to develop a statistical model for the electron energization, which includes the free streaming losses for electrons at energies above $e\Phi_{\parallel}$. Given the pitch angle mixing in the exhaust, the phase space density is assumed to be fully isotropic $f(\mathbf{v}) = f(v)$. To obtain an evolution equation for $f(v)$ we consider the phase-space volume bounded by v_1 and v_2 in Fig. 10. This spherical shell in velocity space has a width $dv = v_2 - v_1$ and a volume $4\pi v_1^2 dv$. The number of electrons in this volume changes because of three effects. 1) Electrons within the losscone of size $4\pi v_1^2 dv R_{\text{loss}}$ are all lost within half a bounce time $\tau_b/2$. 2) Electrons with velocities just below v_2 will be lost by acceleration across the $v = v_2$ boundary. 3) Similarly, electrons with velocities just below v_1 will be accelerated into the volume. Considering a time interval dt , particle conservations may then be expressed as

$$4\pi v^2 dv \left. \frac{\partial f}{\partial t} \right|_{v=v_1} dt = -4\pi v^2 dv f R_{\text{loss}} \frac{dt}{\tau_b/2} \Big|_{v=v_1} - 4\pi v^2 \left. \frac{\partial v}{\partial t} \right|_{v=v_2} dt f \Big|_{v=v_2} + 4\pi v^2 \left. \frac{\partial v}{\partial t} \right|_{v=v_1} dt f \Big|_{v=v_1}.$$

It is clear that the last two terms in the equations above can be rewritten as dv times a differential. Dividing through by $4\pi dv dt$ we then obtain.

$$v^2 \frac{\partial f}{\partial t} = -\frac{2v^2}{\tau_b} f R_{\text{loss}} - \frac{\partial}{\partial v} \left(v^2 \frac{\partial v}{\partial t} f \right). \quad (15)$$

To proceed requires estimations of τ_b and $\partial v/\partial t$ as functions of v . From the trajectory on the right hand side of Fig. 5(c) we conclude that the characteristic orbit length is about $2D$, where (as above) D is the half width of the reconnection exhaust. Then, the orbit bounce time is approximately $\tau_b \simeq 2D/v$. Furthermore, by using $d\mathcal{E}/dt = mv dv/dt$ it follows from Eq. (12) that $\partial v/\partial t \simeq v v_A/(4D)$. Inserting this (and $\tau_b = 2D/v$) into Eq. (15) we obtain

$$4lv^2 \frac{\partial f}{\partial t} + v_A \frac{\partial}{\partial v} (v^3 f) = -4v^3 f R_{\text{loss}}. \quad (16)$$

With the expression in Eq. (14) for $R_{\text{loss}}(v)$ a steady state solution ($\partial f/\partial t = 0$) is then

$$f_{\text{model}} \propto \frac{1}{v^3} \exp \left(-\frac{2B(v - v_{\phi})^2}{B_0 v v_A} \right), \quad (17)$$

applicable for energies above $e\Phi_{\parallel}$ (or $v > v_{\phi}$).

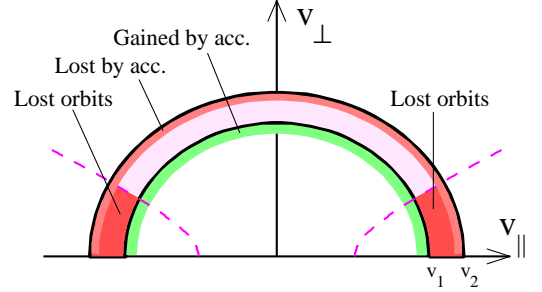


FIG. 10: Regions in velocity space lost or gained by the velocity shell, $v_1 < |\mathbf{v}| < v_2$.

E. Comparison of model for superthermal electrons to kinetic simulation data

To compare Eq. (17) to the kinetic simulation we use the energy distribution f_E , here defined as a function of the relativistic kinetic energy $\mathcal{E} = m_0 c^2 (\gamma - 1)$. Using $n_e = \int f_E d(\gamma - 1) = \int f d^3v$, at non-relativistic energies we have $f_E \propto (\gamma - 1)^{1/2} f$. Fig. 11 shows f_E for the points marked 1 – 3 in Fig. 6, with the most energetic distribution corresponding to point 3, the furthest point away from the x-line. For $m_0 c^2 (\gamma - 1) < e\Phi_{\parallel}$ we approximately have $f_E \propto (\gamma - 1)^{1/2}$ corresponding to $f \simeq \text{const}$ for the near flat-top part of the distributions. For energies above $e\Phi_{\parallel}$ the form in Eq. (17) represents a good approximation to the simulation data.

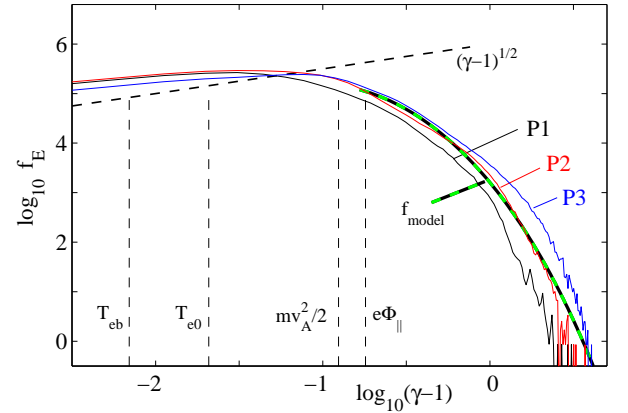


FIG. 11: Electron energy distribution f_E for the points marked P1 – P3 in Fig. 6. For $\mathcal{E} < e\Phi_{\parallel}$ the flattop part of the distribution is observed with $f_E \propto (\gamma - 1)^{1/2}$. The dashed green/black line is f_{model} in Eq. (17) applicable for $\mathcal{E} > e\Phi_{\parallel}$, evaluated with $v_A/c = 0.08$, $e\Phi_{\parallel}/mc^2 = 0.22$ and $B/B_{\infty} = 0.3$.

The distributions in Fig. 11 demonstrate that significant electron energization is possible in an open exhaust of a single X-line reconnection configuration. We find that not only does Φ_{\parallel} provide the electrons with an initial energy boost as they enter the reconnection region,

the structure of E_{\parallel} also reduces the free-streaming along field lines in the reconnection exhaust. This permits the accumulation of energetic electrons, heated mainly by perpendicular electric fields (E_{\perp}) during their repeated bounce-motion across the exhaust. Energization thereby becomes effective throughout the reconnection exhaust at much larger scales than the kinetic length scales of the electrons and ions.

V. COMPARISONS OF NUMERICAL RESULTS WITH SPACECRAFT OBSERVATIONS

A. Electron bulk energization during magnetotail reconnection

Several decades of *in situ* spacecraft observations show that strong kinetic effects are present during magnetic reconnection in the Earth's magnetosphere [37, 39, 40]. Particularly relevant to the role of Φ_{\parallel} are the electron distributions documented by Nagai *et al.*, which, similarly to Fig. 9(a,b), reveal the presence of cold beams directed towards the X-line while energized electrons move away from the reconnection region (see Fig. 4 in Ref. [37]). The importance of these electron beams is also emphasized by measurements taken by the Geotail and the Cluster spacecraft [12, 37, 38]. Within the reconnection outflow the electrons often have a characteristic isotropic flat-top distribution, where the phase space density, f , of the electrons is nearly constant from thermal energies (tens to hundreds of eV) up to several keV. As detailed by Egedal *et al.* [14], the distributions of Fig. 9 resemble closely distributions observed during reconnection events in the magnetotail. Furthermore, the extensive study of flat-top distributions by Asano *et al.* provides the spatial structure of the magnetotail exhausts where these flat-top distributions are observed (see Fig. 22 in Ref. [38]), which resemble the structure of Φ_{\parallel} in Fig. 6).

The kinetic simulation results, the scaling law for Φ_{\parallel} in Eq. (2), and threshold in Eq. (4) for non-adiabatic electron behaviour all suggest that $\beta_{e\infty}$ is an important parameter for the dynamics of the electrons during reconnection. To explore the validity of these results to reconnection in the magnetotail we study the inflow values of β_e as well as Φ_{\parallel} inferred from a number of reconnection events encountered by the Cluster mission.

The four Cluster satellites are moving together in coordinated polar orbits around the Earth, their internal separation changing over the years of operation (year 2000 to present day). The data analyzed here is obtained through the Cluster Active Archive. The magnetic field data is provided by the Flux-Gate Magnetometer (FGM) experiment [41] and the ion plasma data by the Cluster Ion Spectrometry (CIS) experiment [42]. The electron data are from the Plasma Electron and Current Experiment (PEACE) [43]. In the analysis, only the PEACE data points with values above the background electron flux count that were also flagged with quality number 3 or 4

(good for publication) were used. Both the HEEA (high energy sensor) and the LEEA (low energy sensor) data were included. To avoid photo electron measurements we consider only electrons at energy levels higher than 70 eV.

The data selected for our analysis were recorded during encounters with 21 separate magnetic reconnection events in the Earth's magnetotail at about 18 Re. The reconnection events are listed in Ref. [44] along with the signatures of magnetic reconnection, as observed by spacecraft flying through the reconnection region on a path parallel to the magnetotail neutral sheet. During all of the encounters, some or all of the spacecraft observed both reconnection outflow regions. The inflow regions were observed during some of the encounters. The signatures of both inflow and outflow regions are described in Ref. [44]. It must be noted that while the outflow region is easily identified in the data, the inflow region is less distinct and this characteristic may introduce errors.

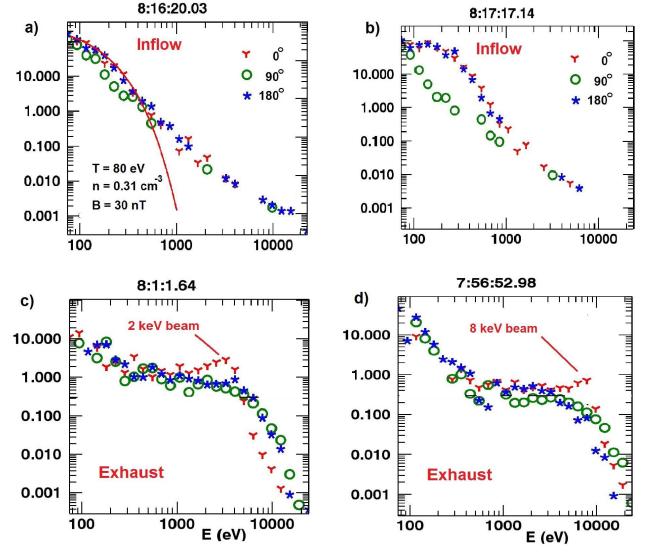


FIG. 12: Characteristic electron distribution functions recorded by the Cluster Mission during a reconnection event on August 21, 2002.

To determine the upstream electron characteristics for the observed magnetic reconnection encounters we considered data recorded by spacecraft during excursions from the outflow regions into areas of lower plasma density and stronger B_x magnetic field. Still, these excursions did not bring the spacecraft into the magnetotail lobe. As an example of the data applied in this analysis, Fig. 12 shows electron phase-space distributions recorded by *Cluster* 4 during a reconnection event encountered on August 21, 2002. The distribution in Fig. 12(a) is representative of the upstream reconnection region, and its thermal component is well described by a Maxwellian fit yielding inflow parameters of $T_e \simeq 80$ eV and $n_e \simeq 0.31$ cm $^{-3}$. At the magnetic field of $B \simeq 30$ nT, the normalized electron pressure for the inflow can then be esti-

mated as $\beta_{e\infty} \simeq 0.011$.

The distribution in Fig. 12(b) is also for a location in the inflow region where the observed electron anisotropy develops in agreement with the kinetic model in Refs. [13, 18]. Meanwhile, the distributions in Figs. 12(c,d) are observed in the exhaust and resemble the numerical distributions of Figs. 9(a,b). Given this resemblance, a local value of $e\Phi_{\parallel}$ can be identified as the energy of the incoming electron beams and/or the energy at which the flattop part of the distributions terminate. By considering all the measured distributions available, the maximal value of Φ_{\parallel} for this event was estimated to be $\Phi_{\parallel} \simeq 9$ keV, corresponding to a normalized potential $e\Phi_{\parallel}/T_e \simeq 110$ similar to the numerical values obtained above.

To obtain the lobe plasma beta values we applied the electron and magnetic field data for the observations of the magnetotail lobe closest in time to the reconnection outflow observations. In table I we provide the values of Φ_{\parallel} , β_{lobe} as well as the inflow values of n_e , T_e , B , and $\beta_{\text{inflow}} (= \beta_{\infty})$ estimated for the reconnection events. Out of the 21 events analyzed, we obtained inflow and lobe plasma beta values for 18 of them using data from the FGM and the PEACE instruments. Compared to the inflow values β_{inflow} characterizing the plasma feeding the reconnection region, the lobe values β_{lobe} were typically lower by an order of magnitude.

The results from the described analysis of the Cluster data are summarized in Fig. 13, which provides the values of $e\Phi_{\parallel}/T_e$ as a function of $\beta_{e\infty}$. For comparison, the red symbols represent the range of $e\Phi_{\parallel}/T_e$ recorded in the numerical simulations (with values from particular figures above indicated). In addition, the blue line is $e\Phi_{\parallel}/T_e$ of Eq. (2), which yields a lower bound for the observations and simulations.

The range of $e\Phi_{\parallel}/T_e$ from the simulation presented here (with $\beta_{e\infty} = 0.003$) is in good agreement with the spacecraft observations. However, the spacecraft data suggest that the transition to the regime influenced by electron holes and double layers (large values of $e\Phi_{\parallel}/T_e$) occurs at $\beta_{e\infty} \simeq 0.1$. In contrast, all simulations we have studied with $\beta_{e\infty} \simeq 0.1$ are well described by Eq. (2) (the blue line) [22]. Nevertheless, the threshold for the transition to non-adiabatic inflow electron, $\beta_{e\infty} < 0.02$ in Eq. (4), is in reasonable agreement with the spacecraft observations.

B. Superthermal electrons in the magnetotail

In a previous study of magnetotail observations we found that superthermal electrons often acquire a constant energy-gain, $\Delta\mathcal{E}$, independent of their initial energy [45]. As an example, in Fig. 14 we provide measurements of superthermal electrons recorded by the Cluster Mission during the much studied October 1, 2001 reconnection event [46]. Time series measurements by the RAPID instrument are given in a). For the selected time points for which the distributions are shown in b), we apply a

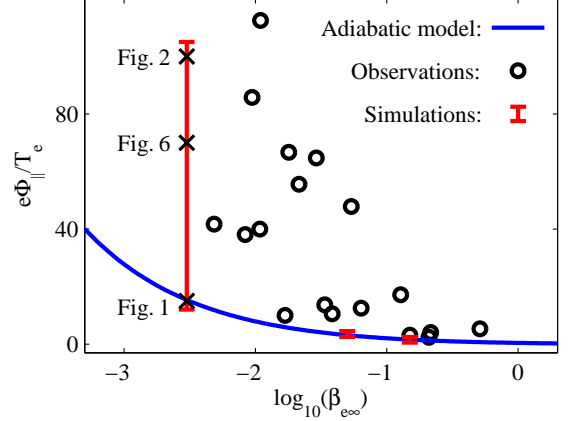


FIG. 13: Values of $e\Phi_{\parallel}/T_e$ as a function of $\beta_{e\infty}$. The black circles are calculated based on the values in Table I inferred from Cluster spacecraft data. The red symbols represent values of kinetic simulations. The values of $e\Phi_{\parallel}/T_e$ for $\beta_{e\infty} = 0.05$ and 0.15 are from simulations presented in Ref. [22]. The blue line is the adiabatic model in Eq. (2). This model does not include the effects on Φ_{\parallel} caused by electron holes and double layers, and thus represents a lower theoretical bound for $e\Phi_{\parallel}/T_e$.

TABLE I: Plasma beta and guide field values for magnetic reconnection inflow regions and the lobe.

Date	$\Phi_{\parallel}/\text{kV}$	β_{lobe}	T_e/eV	n_e/cm^{-3}	B/nT	β_{inflow}
2001 08 22	8	0.003	210	0.07	26	0.008
2001 09 10	0.8	0.003	340	0.36	15	0.21
2001 09 12	5	0.001	90	0.25	20	0.026
2001 10 01	10	0.008	150	0.28	30	0.018
2001 10 08	2	0.004	500	0.45	20	0.22
2001 10 11	2	0.03	650	0.14	15	0.15
2002 08 21	9	0.003	80	0.32	30	0.011
2002 08 28	2.1	0.0003	200	0.2	20	0.038
2002 09 13	3	0.001	220	0.23	24	0.034
2002 09 18	11	0.0009	230	0.24	20	0.054
2002 10 02	11	0.002	170	0.064	12	0.030
2003 08 17	5	0.0003	120	0.17	40	0.0048
2003 08 24	6	0.0006	350	0.38	20	0.13
2003 09 19	8	0.002	1500	0.2	15	0.51
2003 10 04	6	0.003	70	0.14	20	0.0094
2003 10 09	5	0.002	400	0.12	17	0.064
2004 09 14	6	0.002	150	0.075	20	0.011
2005 09 26	1	0.001	100	0.70	40	0.017

Liouville mapping technique to obtain the energy gains shown in c). Again, more details of this analysis are giving in Ref. [45].

For all the events analyzed it is found that, for the most energetic electrons, $\Delta\mathcal{E}$ is constant, independent of the initial energy. In Ref. [45] we then concluded that the energization of the superthermal electrons is set by $e\Phi_{\parallel}$, but our understanding of this has changed and is now very different. From the above analysis it is clear that it

is the bulk-energization (including flat-top distributions) that is controlled by $e\Phi_{\parallel}$, and the observed superthermal electrons energization is better described by Eq. (12), allowing for energization to energies much larger than $e\Phi_{\parallel}$. However, because of the initial hard power-law spectrum $f(v) \propto v^{-3}$ of incoming lobe electrons and because $\Delta\mathcal{E}$ in Eq. (12) is proportional to the initial energy, the present 2D model predicts superthermal electrons in excess of the observations. This discrepancy can be explained by the finite y -extent of the magnetotail. In a realistic application, the effectiveness of the present model needs to be limited, as the maximum energization level is set by the potential drop along the extent of the reconnection x-line. The constant levels of $\Delta\mathcal{E}$ deduced in the analysis of Ref. [45] are then consistent with our superthermal heating mechanism in combination with a finite dusk-dawn (or for observations: dusk - spacecraft) potential drop during magnetotail reconnection.

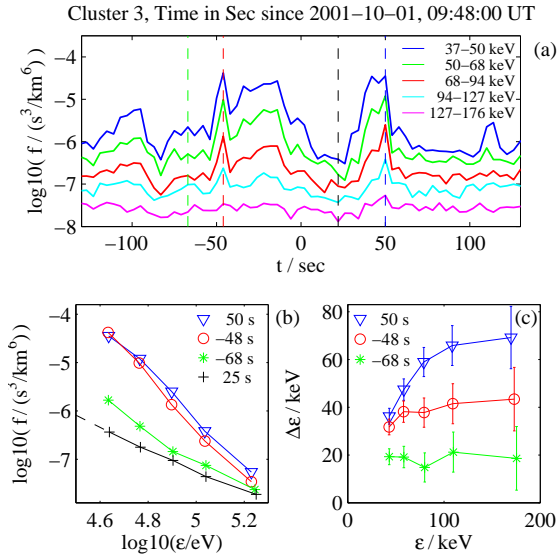


FIG. 14: Electron phase-space densities from the RAPID measurement on Cluster 3. (b) Electron distribution observed at separate time points. (c) Spectra of $\Delta\mathcal{E}$ for three selected times. The observed spectra of $\Delta\mathcal{E}$, independent of \mathcal{E} for large \mathcal{E} , are consistent with Eq. (12) when taking into account the finite extent of the systems in the magnetotail y -direction.

C. Solar flares

Compelling observational evidence exists for confinement of energetic electrons by parallel electric fields during solar flare events. This evidence is summarized in papers by Li. *et al.*, [16, 29, 30] who (as mentioned above) explored the role of double layers for reducing the free streaming losses of reconnection energized electrons along the field lines. The evidence includes the formation of energetic electron populations detected in the vicinity of the expected loop-top reconnection sites. The lifetime

of these energetic populations are inferred to be much longer than the thermal electron transit time [1], suggesting that parallel electric fields must be important to reduce free streaming losses along magnetic field lines.

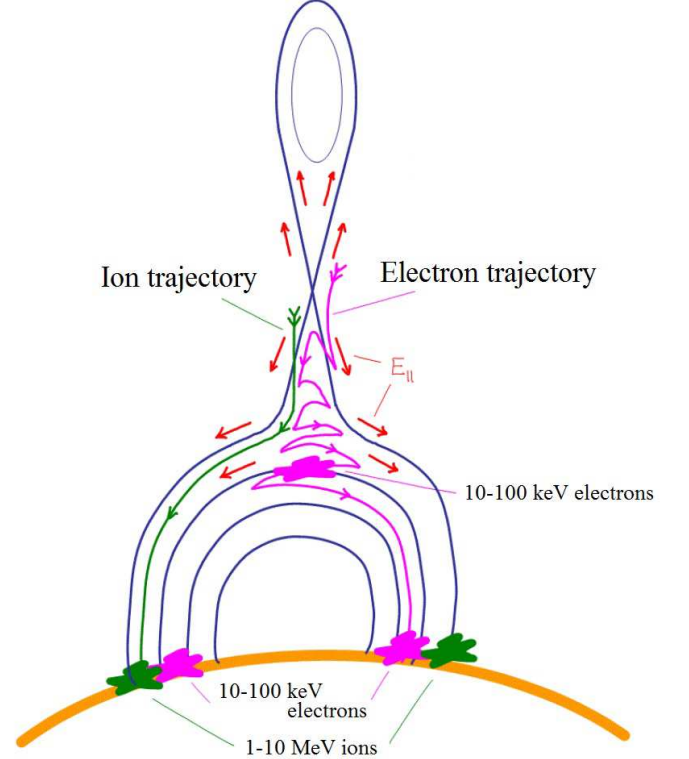


FIG. 15: Schematic model of a solar flare

Based on the Masuda flare model [47], Fig. 15 provides a schematic illustration of the electric and magnetic geometry suggested by the observations and required for confinement of electrons by parallel electric fields. Again, the analysis by Li. *et al.* and also earlier authors (see references in Ref. [16]) have already suggested that electric fields in double layers may help confine the energized electrons. In addition, the present analysis suggests that the parallel electric fields are not only important for confining the electrons but are an integral component to the overall energization processes. For example, the observed and remarkably efficient energization of the bulk electrons from about 1keV up to 10-100keV [1] is consistent with the development of an acceleration potential with a magnitude of $e\Phi_{\parallel}/T_e = 100$ seen in the magnetotail and in our simulation. In addition, the most energetic electrons reaching the MeV energy range can also be accounted for by Eq. (17). In fact, for energies just above $e\Phi_{\parallel}$, Eq. (17) yields a hard powerlaw spectrum $f(v) \propto v^{-3}$ for about an order of magnitude in energy, sufficient to explain the most energetic electrons in the solar flare observations. We also note that the $\beta_{e\infty}$ -threshold ($\beta_{e\infty} < 0.02$) for the non-adiabatic electron dynamics to occur is easily satisfied in solar flare events [15].

In our model, the electrons are only energized by Φ_{\parallel} as they enter the reconnection exhaust. Meanwhile, ions will be accelerated away from the reconnection region by these parallel electric fields. The path of the ions will not coincide with instantaneous magnetic field lines, and a fraction of the ions are likely to endure acceleration by E_{\parallel} to much larger values than $e\Phi_{\parallel}$ during their transit through the reconnection exhaust. This may account for the energization of ions in the range of 10 MeV recorded by the RHESSI spacecraft [48]. Of course, it must be noted that our numerical simulation covers a domain size of about $300d_i$, whereas the size of a solar flare is about 10^7d_i . Furthermore, solar flares are believed to include a guide magnetic field of order unity, whereas the present simulation is for anti-parallel reconnection. Nevertheless, we expect that the described general processes leading to non-adiabatic parallel electron dynamics and strong electron energization will also be applicable to reconnection in very large systems.

VI. CONCLUSIONS

The heating by $\mathbf{E} \cdot \mathbf{v}_D$ has been found generic to plasma flows driven by magnetic tension [36] and is common to a range of models for electron energization. An example is Drake's Fermi acceleration model considering a bath of reconnecting magnetic islands [49]. Likewise the term $\mathbf{E} \cdot \mathbf{v}_D$ is also responsible for driving powerlaw distributions in highly relativistic pair plasmas [50]. A third example is the energization documented while propagating test-particles through the fields of Ideal-MHD simulations [51], where confinement may occur when electrons bounce between dipolarization fronts and the stronger magnetic fields close to Earth [51, 52]. However, Ideal-MHD assumes $E_{\parallel} = 0$ and the described effects of localized electron trapping and the initial energization by E_{\parallel} are therefore omitted.

The key new feature presented here is the importance of the magnetic field aligned electric fields E_{\parallel} for initial energization of the electrons. Because the subsequent energization by E_{\perp} is proportional to \mathcal{E} , the initial energy boost that electrons acquire from $e\Phi_{\parallel}$ largely determines the overall efficiency of the energization process. The large amplitude structure of Φ_{\parallel} also limits the free streaming particle losses along magnetic field lines, which is essential for confining the electrons and shaping the spectra of their energy distribution. The heating is effective in the full exhaust of a single X-line configuration, and does not require pressure anisotropy to develop.

The large values of E_{\parallel} are observed within density cavities and develop in association with the strong double layers. A threshold, $\beta_{e\infty} < 0.02$ is derived for the strong double layer formation, suggesting that these are likely to be present during solar flare events. Indeed, the level of electron energization observed in the simulation is consistent with that observed during solar flares. Furthermore, we show the details of the electron distribution functions

described in our analysis are in agreement with *in situ* spacecraft measurements obtained over the last decade during reconnection events in the Earth's magnetotail.

Acknowledgments

The work at UW-Madison was funded in part by NASA grant NNX14AC68G. The numerical simulation work was supported by the NASA Heliophysics Theory Program at LANL. Initial simulations were carried out using LANL institutional computing resources and the Pleiades computer at NASA, while the final simulation was carried out on Kraken with an allocation of advanced computing resources provided by the National Science Foundation at the National Institute for Computational Sciences (<http://www.nics.tennessee.edu/>).

Appendix A: Use of the guiding center model for estimating the electron energization rate

In this appendix we first discuss why the guiding center model can provide an accurate prediction of the electron heating rate for the pitch angle mixed exhaust. We then estimate the heating rate based on this model and recover result given above in Eq. (12). We thereby validate the above estimate and highlight the similarity (and differences) between the results in the present paper compared to those of earlier works using the guiding center model [35].

From Fig. 7(b) above it is clear that the main heating source of the electrons is the perpendicular electric fields, and thus, the local heating results from the term $en_e \mathbf{V}_{e\perp} \cdot \mathbf{E}$, where $\mathbf{V}_{e\perp}$ is the electron fluid velocity also appearing in the electron momentum equation:

$$\mathbf{E} + \mathbf{V}_e \times \mathbf{B} = -\nabla \cdot \bar{\mathbf{P}}_e / (en_e) \quad . \quad (18)$$

Due to the low values of B in the exhaust, the magnetic moments of the electrons are not conserved. The particle motion therefore becomes chaotic and all pitch angle information is lost as electrons pass through the midplane. We are therefore only interested in the average electron behavior as a function of energy. It is clear that the guiding center approximation with the drifts $\mathbf{v}_D = \mathbf{v}_k + \mathbf{v}_{\nabla B}$ does not formally apply (where $\mathbf{v}_k = m_e v_{\parallel}^2 \mathbf{B} \times \kappa / (eB^2)$ with $\kappa = \mathbf{b} \cdot \nabla \mathbf{b}$ is the curvature drift and $\mathbf{v}_{\nabla B} = m_e v_{\perp}^2 \mathbf{B} \times \nabla B / (2eB^2)$ is the gradient-B drift). Nevertheless, by direct evaluation of the expression $en_e \mathbf{V}_{e\perp} \cdot \mathbf{E} = e \int \mathbf{v}_D f d^3v + \nabla \times \mathbf{M}$, with the magnetization $e\mathbf{M} = \mathbf{b} \int \mu f d^3v$, it is well known that $\mathbf{V}_{e\perp}$ in Eq. (18) is recovered for the relevant limit where $\bar{\mathbf{P}}_e$ has no off diagonal stress [53]. Therefore, although the guiding center approximation does not account for the chaotic motion of the individual electrons, it does accurately predict the total fluid drift. Furthermore, the predicted contribution to $\mathbf{V}_{e\perp}$ from particles within a

given energy interval is also accurate. The guiding center approximation thus allows us to estimate the average electron drift (and associated energization) as a function of energy.

To derive an expression for $d\mathcal{E}/dt$ using the guiding center model, we note that previous studies in similar geometries have found that curvature drifts dominate the particle motion in the direction of the reconnection electric field [35]. Therefore, we here estimate the energy changes over a single bounce orbit caused by the curvature drift, $\Delta\mathcal{E} = e \int_0^{\tau_b} \mathbf{v}_k \cdot \mathbf{E}_{\text{rec}} dt$. Using $|\kappa| = 1/R_c$ where R_c is the radius of curvature for the magnetic field line and $\tau_b \simeq \pi R_c/v_{\parallel}$ we obtain $\Delta\mathcal{E} \simeq E_{\text{rec}} \pi m_e |v_{\parallel}|/B \simeq E_{\text{rec}} m v/B$, as the average energization per bounce. Us-

ing $E_{\text{rec}} \simeq v_A B_0/10$ we obtain

$$\frac{d\mathcal{E}}{dt} = \frac{\Delta\mathcal{E}}{\tau_b} \simeq \frac{v_A B_0}{10} \frac{m v}{B \tau_b} \simeq \frac{v_A}{l_{\text{orb}}} m v^2, \quad (19)$$

where we have used $B \simeq B_0/10$. Thus, we find that

$$\frac{d\mathcal{E}}{dt} \simeq \frac{2v_A}{l_{\text{orb}}} \mathcal{E}. \quad (19)$$

This order of magnitude estimate of the heating rate is consistent with the result in Sec. III D. In fact, taking the orbit length as four times the half exhaust width, $l_{\text{orb}} = 4D$, we recover the expression in Eq. (12).

-
- [1] S. Krucker, H. S. Hudson, L. Glesener, S. M. White, S. Masuda, J.-P. Wuelser, and R. P. Lin, “Measurements of the Coronal Acceleration Region of a Solar Flare,” *Astrophys. J.*, vol. 714, pp. 1108–1119, May 2010.
- [2] M. Øieroset, T. Phan, M. Fujimoto, R. P. Lin, and R. P. Lepping, “In situ detection of collisionless reconnection in the earth’s magnetotail,” *Nature*, vol. 412, pp. 414–417, JUL 26 2001.
- [3] J. F. Drake, M. Swisdak, H. Che, and M. A. Shay, “Electron acceleration from contracting magnetic islands during reconnection,” *Nature*, vol. 443, pp. 553–556, OCT 5 2006.
- [4] M. Oka, T. D. Phan, S. Krucker, M. Fujimoto, and I. Shinohara, “ELECTRON ACCELERATION BY MULTI-ISLAND COALESCENCE,” *ASTROPHYSICAL JOURNAL*, vol. 714, pp. 915–926, MAY 1 2010.
- [5] M. Hoshino, “Stochastic Particle Acceleration in Multiple Magnetic Islands during Reconnection,” *Phys. Rev. Lett.*, vol. 108, MAR 28 2012.
- [6] J. F. Drake, M. Swisdak, and R. Fermo, “THE POWER-LAW SPECTRA OF ENERGETIC PARTICLES DURING MULTI-ISLAND MAGNETIC RECONNECTION,” *ASTROPHYSICAL JOURNAL LETTERS*, vol. 763, JAN 20 2013.
- [7] L. J. Chen, A. Bhattacharjee, P. A. Puhl-Quinn, H. Yang, N. Bessho, S. Imada, S. Muehlbachler, P. W. Daly, B. Lefebvre, Y. Khotyaintsev, A. Vaivads, A. Fazakerley, and E. Georgescu, “Observation of energetic electrons within magnetic islands,” *Nature Physics*, vol. 4, pp. 19–23, JAN 2008.
- [8] M. Øieroset, T. D. Phan, J. P. Eastwood, M. Fujimoto, W. Daughton, M. A. Shay, V. Angelopoulos, F. S. Mozer, J. P. McFadden, D. E. Larson, and K. H. Glassmeier, “Direct Evidence for a Three-Dimensional Magnetic Flux Rope Flanked by Two Active Magnetic Reconnection X Lines at Earth’s Magnetopause,” *Phys. Rev. Lett.*, vol. 107, OCT 13 2011.
- [9] L. BLOCK, “Double-layer review,” *ASTROPHYSICS AND SPACE SCIENCE*, vol. 55, no. 1, pp. 59–83, 1978.
- [10] N. SINGH, H. THIEMANN, and R. SCHUNK, “Electric fields and double-layers in plasmas,” *LASER AND PARTICLE BEAMS*, vol. 5, pp. 233–255, MAY 1987.
- [11] M. RAADU and J. RASMUSSEN, “Dynamical aspects of electrostatic double-layers,” *ASTROPHYSICS AND SPACE SCIENCE*, vol. 144, pp. 43–71, MAY 1988.
- [12] L. J. Chen, N. Bessho, B. Lefebvre, H. Vaith, A. Fazakerley, A. Bhattacharjee, P. A. Puhl-Quinn, A. Runov, Y. Khotyaintsev, A. Vaivads, E. Georgescu, and R. Torbert, “Evidence of an extended electron current sheet and its neighboring magnetic island during magnetotail reconnection,” *J. Geophys. Res.*, vol. 113, DEC 19 2008.
- [13] J. Egedal, W. Fox, N. Katz, M. Porkolab, M. Øieroset, R. P. Lin, W. Daughton, and D. J. F., “Evidence and theory for trapped electrons in guide field magnetotail reconnection,” *J. Geophys. Res.*, vol. 113, p. A12207, MAR 25 2008.
- [14] J. Egedal, W. Daughton, and A. Le, “Large-scale electron acceleration by parallel electric fields during magnetic reconnection,” *Nature Physics*, vol. 8, pp. 321–324, APR 2012.
- [15] L. Fletcher, B. R. Dennis, H. S. Hudson, S. Krucker, K. Phillips, A. Veronig, M. Battaglia, L. Bone, A. Caspi, Q. Chen, P. Gallagher, P. T. Grigis, H. Ji, W. Liu, R. O. Milligan, and M. Temmer, “An observational overview of solar flares,” *Space Science Reviews*, vol. 159, pp. 19–106, SEP 2011.
- [16] T. C. Li, J. F. Drake, and M. Swisdak, “Suppression of energetic electron transport in flares by double layers,” *Astrophys. J.*, vol. 757, SEP 20 2012.
- [17] A. Le, J. Egedal, W. Daughton, W. Fox, and N. Katz, “Equations of State for Collisionless Guide-Field Reconnection,” *Phys. Rev. Lett.*, vol. 102, FEB 27 2009.
- [18] J. Egedal, A. Le, and W. Daughton, “A review of pressure anisotropy caused by electron trapping in collisionless plasma, and its implications for magnetic reconnection,” *Phys. Plasmas*, vol. 20, JUNE 2013.
- [19] K. Bowers, B. Albright, L. Yin, W. Daughton, V. Roytershteyn, B. Bergen, and T. Kwan, “Advances in petascale kinetic plasma simulation with VPIC and Roadrunner,” *Journal of Physics: Conference Series*, vol. 180, p. 012055 (10 pp.), 2009 2009.
- [20] J. Egedal, W. Daughton, J. F. Drake, N. Katz, and A. Le, “Formation of a localized acceleration potential during magnetic reconnection with a guide field,” *Phys. Plasmas*, vol. 16, MAY 2009.
- [21] G. F. Chew, M. L. Goldberger, and F. E. Low, “The boltzmann equation and the one-fluid hydromagnetic equations in the absence of particle collisions,”

- Proc. Royal Soc. A*, vol. 112, p. 236, 1956.
- [22] A. Le, J. Egedal, W. Daughton, J. F. Drake, W. Fox, and N. Katz, "Magnitude of the Hall fields during magnetic reconnection," *Geophys. Res. Lett.*, vol. 37, FEB 11 2010.
 - [23] J. Ng, J. Egedal, A. Le, W. Daughton, and L. J. Chen, "Kinetic structure of the electron diffusion region in antiparallel magnetic reconnection," *Phys. Rev. Lett.*, vol. 106, FEB 10 2011.
 - [24] D. GURNETT and L. FRANK, "Region of intense plasma-wave turbulence on auroral field lines," *J. Geophys. Res.*, vol. 82, no. 7, pp. 1031–1050, 1977.
 - [25] H. MATSUMOTO, H. KOJIMA, T. MIYATAKE, Y. OMURA, M. OKADA, I. NAGANO, and M. TSUTSUI, "Electrostatic solitary waves (esw) in the magnetotail - ben wave-forms observed by geotail," *Geophys. Res. Lett.*, vol. 21, pp. 2915–2918, DEC 15 1994.
 - [26] R. E. Ergun, L. Andersson, J. Tao, V. Angelopoulos, J. Bonnell, J. P. McFadden, D. E. Larson, S. Eriksson, T. Johansson, C. M. Cully, D. N. Newman, M. V. Goldman, A. Roux, O. LeContel, K. H. Glassmeier, and W. Baumjohann, "Observations of Double Layers in Earth's Plasma Sheet," *Phys. Rev. Lett.*, vol. 102, APR 17 2009.
 - [27] L. Andersson, R. E. Ergun, J. Tao, A. Roux, O. LeContel, V. Angelopoulos, J. Bonnell, J. P. McFadden, D. E. Larson, S. Eriksson, T. Johansson, C. M. Cully, D. L. Newman, M. V. Goldman, K. H. Glassmeier, and W. Baumjohann, "New Features of Electron Phase Space Holes Observed by the THEMIS Mission (vol 102, art no 225004, 2009)," *Phys. Rev. Lett.*, vol. 103, JUL 31 2009.
 - [28] F. S. Mozer, S. D. Bale, J. W. Bonnell, C. C. Chaston, I. Roth, and J. Wygant, "Megavolt Parallel Potentials Arising from Double-Layer Streams in the Earth's Outer Radiation Belt," *Phys. Rev. Lett.*, vol. 111, DEC 2 2013.
 - [29] T. C. Li, J. F. Drake, and M. Swisdak, "Coronal electron confinement by double layers," *ASTROPHYSICAL JOURNAL*, vol. 778, DEC 1 2013.
 - [30] T. C. Li, J. F. Drake, and M. Swisdak, "Dynamics of double layers, ion acceleration, and heat flux suppression during solar flares," *ASTROPHYSICAL JOURNAL*, vol. 793, SEP 20 2014.
 - [31] M. Shay, J. Drake, M. Swisdak, and B. Rogers, "The scaling of embedded collisionless reconnection," *Phys. Plasmas*, vol. 11, pp. 2199–2213, MAY 2004.
 - [32] M. Shay, J. Drake, B. Rogers, and R. E. Denton, "Alfvenic collisionless magnetic reconnection and the hall term," *J. Geophys. Res.*, vol. 106, pp. 3759–3772, MAR 1 2001.
 - [33] A. Le, J. Egedal, J. Ng, H. Karimabadi, J. Scudder, V. Roytershteyn, W. Daughton, and Y. H. Liu, "Current sheets and pressure anisotropy in the reconnection exhaust," *Phys. Plasmas*, vol. 21, JAN 2014.
 - [34] J. Buchner and L. Zelenyi, "Regular and chaotic charged-particle motion in magnetotail-like field reversals .1. basic theory of trapped motion," *J. Geophys. Res.*, vol. 94, pp. 11821–11842, SEP 1 1989.
 - [35] J. T. Dahlin, J. F. Drake, and M. Swisdak, "The mechanisms of electron heating and acceleration during magnetic reconnection," *Phys. Plasmas*, vol. 21, SEP 2014.
 - [36] A. Beresnyak and H. Li, "First order particle acceleration in magnetically-driven flows," *submitted to PRL*, 2014.
 - [37] T. Nagai, I. Shinohara, M. Fujimoto, M. Hoshino, Y. Saito, S. Machida, and T. Mukai, "Geotail observations of the hall current system: Evidence of magnetic reconnection in the magnetotail," *J. Geophys. Res.*, vol. 106, pp. 25929–25949, NOV 1 2001.
 - [38] Y. Asano, R. Nakamura, I. Shinohara, M. Fujimoto, T. Takada, W. Baumjohann, C. J. Owen, A. N. Fazakerley, A. Runov, T. Nagai, E. A. Lucek, and H. Reme, "Electron flat-top distributions around the magnetic reconnection region," *J. Geophys. Res.*, vol. 113, JAN 24 2008.
 - [39] L. R. P., A. K. A., A. S., C. C., C. D., E. R., L. D., M. J., M. M., P. G. K., R. H., B. J. M., C. J., C. F., D. C., W. K. P., S. T. R., H. J., R. J. C., and P. G., "A 3-dimensional plasma and energetic particle investigation for the wind spacecraft," *Space Science Reviews*, vol. 71, pp. 125–153, FEB 1995.
 - [40] M. Øieroset, R. Lin, and T. Phan, "Evidence for electron acceleration up to 300 keV in the magnetic reconnection diffusion region of earth's magnetotail," *Phys. Rev. Lett.*, vol. 89, p. 195001, NOV 4 2002.
 - [41] A. Balogh, C. M. Carr, M. H. Acuña, M. W. Dunlop, T. J. Beek, P. Brown, K.-H. Fornacon, E. Georgescu, K.-H. Glassmeier, J. Harris, G. Musmann, T. Oddy, and K. Schwingenschuh, "The Cluster Magnetic Field Investigation: overview of in-flight performance and initial results," *Annales Geophysicae*, vol. 19, pp. 1207–1217, 2001.
 - [42] H. Reme, C. Aoustin, M. Bosqued, I. Dandouras, B. Lavraud, J. Sauvaud, A. Barthe, J. Bouyssou, T. Camus, O. Coeur-Joly, A. Cros, J. Cuvelo, F. Ducay, Y. Garbarowitz, J. Medale, E. Penou, H. Perrier, D. Romefort, J. Rouzaud, C. Vallat, D. Alcayde, C. Jacquey, C. Mazelle, C. d'Uston, E. Mobius, L. Kistler, K. Crocker, M. Granoff, C. Mouikis, M. Popecki, M. Vossbury, B. Klecker, D. Hovestadt, H. Kucharek, E. Kueneth, G. Paschmann, M. Scholer, N. Sckopke, E. Seiden-schwang, C. Carlson, D. Curtis, C. Ingraham, R. Lin, J. McFadden, G. Parks, T. Phan, V. Formisano, E. Amata, M. Bavassano-Cattaneo, P. Baldetti, R. Bruno, G. Chionchio, A. Di Lellis, M. Marcucci, G. Pallochia, A. Korth, P. Daly, B. Graeve, H. Rosenbauer, V. Vasyliunas, M. McCarthy, M. Wilber, L. Eliasson, R. Lundin, S. Olsen, E. Shelley, S. Fuselier, A. Ghielmetti, W. Lennartsson, C. Escoubet, H. Balsiger, R. Friedel, J. Cao, R. Kovrazhkin, I. Papamastorakis, R. Pellat, J. Scudder, and B. Sonnerup, "First multi-spacecraft ion measurements in and near the Earth's magnetosphere with the identical Cluster ion spectrometry (CIS) experiment," *ANNALES GEOPHYSICAE*, vol. 19, pp. 1303–1354, OCT-DEC 2001.
 - [43] A. D. Johnstone, C. Alsop, S. Burge, P. J. Carter, A. J. Coates, A. J. Coker, A. N. Fazakerley, M. Grande, R. A. Gowen, C. Gurgiolo, B. K. Hancock, B. Narheim, A. Preece, P. H. Sheather, J. D. Winningham, and R. D. Woodliffe, "Peace: A plasma electron and current experiment," *Space Sci. Rev.*, vol. 79, pp. 351–398, JAN 1997.
 - [44] A. L. Borg, M. G. G. T. Taylor, and J. P. Eastwood, "Observations of magnetic flux ropes during magnetic reconnection in the Earth's magnetotail," *ANNALES GEOPHYSICAE*, vol. 30, no. 5, pp. 761–773, 2012.
 - [45] J. Egedal, A. Le, Y. Zhu, W. Daughton, M. Øieroset, T. Phan, R. P. Lin, and J. P. Eastwood, "Cause of super-thermal electron heating during magnetotail reconnection," *Geophys. Res. Lett.*, vol. 37, MAY 28 2010.
 - [46] J. R. Wygant, C. A. Cattell, R. Lysak, Y. Song, J. Dombeck, J. McFadden, F. S. Mozer, C. W. Carlson,

- G. Parks, E. A. Lucek, A. Balogh, M. Andre, H. Reme, M. Hesse, and C. Mouikis, "Cluster observations of an intense normal component of the electric field at a thin reconnecting current sheet in the tail and its role in the shock-like acceleration of the ion fluid into the separatrix region," *J. Geophys. Res.*, vol. 110, SEP 3 2005.
- [47] S. Masuda, T. Kosugi, H. Hara, and Y. Ogawaray, "A loop top hard x-ray source in a compact solar-flare as evidence for magnetic reconnection," *Nature*, vol. 371, pp. 495–497, OCT 6 1994.
- [48] R. P. Lin, S. Krucker, G. J. Hurford, D. M. Smith, and H. S. Hudson, "RheSSI observations of particle acceleration and energy release in an intense solar gamma-ray line flare," *Astrophys. J.*, vol. 595, pp. L69–L76, 2003.
- [49] J. F. Drake, M. A. Shay, W. Thongthai, and M. Swisdak, "Production of energetic electrons during magnetic reconnection," *Phys. Rev. Lett.*, vol. 94, p. 095001, MAR 11 2005.
- [50] Fan Guo, Hui Li, W. Daughton, and Yi-Hsin Liu, "Formation of Hard Power Laws in the Energetic Particle Spectra Resulting from Relativistic Magnetic Reconnection," *Phys. Rev. Lett.*, vol. 113, p. 155005 (5 pp.), 10 Oct. 2014.
- [51] J. Birn, M. Hesse, R. Nakamura, and S. Zaharia, "Particle acceleration in dipolarization events," *J. Geophys. Res.*, vol. 118, pp. 1960–1971, MAY 2013.
- [52] A. Runov, V. Angelopoulos, X.-Z. Zhou, X. J. Zhang, S. Li, F. Plaschke, and J. Bonnell, "A THEMIS multicasestudy of dipolarization fronts in the magnetotail plasma sheet," *J. Geophys. Res.*, vol. 116, MAY 24 2011.
- [53] R. D. Hazeltine and J. D. Meiss, *Plasma Confinement*. Addison-Wesley, 1992.